

**Experimental and Computational Study of
Multi-phase Fluid Flow in Nozzle and Mold
during Continuous Slab Casting**

By

Go-Gi Lee

Department of Materials Science and Engineering
(Steelmaking Process Program)
Pohang University of Science and Technology

A thesis is submitted to the faculty of Pohang University of
Science and Technology in partial fulfillment of the
requirements for the degree of Doctor of Philosophy in the field
of Materials Science and Engineering

Pohang, Korea

June 4, 2008

Approved by

Prof. Seon-Hyo Kim

Table of contents

List of Figures

List of Tables

CHAPTER 1. Introduction

- 1.1 Background
- 1.2 Objective of this study
- 1.3 Methodology for this study

CHAPTER 2. Experimental

- 2.1 Plant measurements
 - 2.1 Nail board dip test
 - A. Experimental procedure
 - B. Results
 - 2.2 Particle entrapment near subsurface hook region in slabs
 - A. Introduction
 - B. Experimental procedure
 - C. Results
 - 2.3 Particle entrapment in internal region in slabs
 - A. Introduction
 - B. Experimental procedure
 - C. Results
 - 2.4 Summary
- 2.2 Water model experiments for initial bubble behavior
 - 2.2.1 Introduction

- 2.2.2 Experimental procedure
- 2.2.3 Active sites measurements on refractory surface
 - A. Stagnant flow
 - B. Downward flowing
 - C. Inner wall surface of real upper tundish nozzle
 - D. Bubble behavior in downward-flowing water
 - E. Bubble size prediction in liquid steel
- 2.2.4 Surface coating of porous refractory
- 2.2.5 Summary

CHAPTER 3. Computational Modeling of Fluid Flow

- 3.1 Governing equations for fluid flow
- 3.2 Bubbles in fluid flow
 - 3.2.1 Drag force
 - 3.2.2 Shear lift force
 - 3.2.3 Gravitational force
- 3.3 Boundary conditions
 - 3.3.1 Nozzle inlet
 - 3.3.2 Nozzle and mold outlet
 - 3.3.3 Mold inlet
 - 3.3.4 Wall
 - 3.3.5 Solution procedure
- 3.4 Fluid flow in nozzle
- 3.5 Fluid flow in mold
- 3.6 Summary

CHAPTER 4. Conclusions

Summary (in Korean)

Reference

List of Figures

- 1.1 Schematic of phenomena in the mold region of a steel slab caster
- 1.2 Typical curved hook shape
- 1.3 Surface defects due to entrapment of bubble and inclusions resulting in (a) blister, and (b) sliver
- 1.4 Wide variations of entrapped bubble in slabs: (a) subsurface region, and (b) internal region
- 2.1 (a) Schematic diagram of nail board, (b) an example of aluminum and stainless steel nails and (c) close view of the stainless steel nail showing solidified lump, which reveal surface velocity
- 2.2 Measured mold slag layer thickness, steel meniscus profile, and surface flow direction according to the gas volume fraction at UTN: (a) 3.63%, (b) 4.84%, (c) 7.00%, and (d) 8.73%
- 2.3 Schematic illustrating formation of curved hooks in ULC steel slabs by meniscus solidification and subsequent liquid steel overflow
- 2.4 Sample I (a) location obtained from slab corner and (b) three different horizontal sections cut for microscopy analysis of hooks and oscillation mark shown in circles
- 2.5 Sample II (a) location obtained from slab corners and (b) location of sections cut for microscopy analysis showing oscillation mark shape
- 2.6 Sample III (a) location obtained from slab corners and (b) ~ (d) orientation of three different vertical sections cut for microscopy analysis
- 2.7 Optical micrographs of horizontal cross sections (Sample I) showing evidence of liquid steel overflow
- 2.8 Optical micrographs at different distances from wide face (sample II) showing line of frozen meniscus origin: “hooks”
- 2.9 Line of frozen meniscus origins obtained from micrograph analysis of Sample II (a) and (b) 3-D shape of frozen meniscus hook at 2nd OM
- 2.10 Top views of lines of frozen meniscus origins (hooks) from micrographs (Sample II) showing hook depth increase around corner and explanation of hook depth variations observed in micrographs
- 2.11 Hook shapes (lines of frozen meniscus from vertical sections through sample III) (a) micrograph of 45 degree section and (b) shapes traced from three different hooks
- 2.12 Lines of frozen meniscus (sample II) at three locations around slab perimeter of narrow face, showing increase in hook size towards corner
- 2.13 Hook depth variation along mold perimeter of (a) narrow face and (b) wide face
- 2.14 Figure 2.14 (a) Schematic of sample locations and surfaces of particle analysis for each test in Table 2.1, and the result of (b) the signal map using ultrasonic

- analysis
- 2.15 Locations of entrapped particles in slab samples with casting conditions shown in Table 1: (a) low gas flow rate, (b) high gas flow rate
 - 2.16 Shell thickness prediction in the mold by CON1D
 - 2.17 Schematic of 1/3 water model experiment
 - 2.18 Gas injection through porous MgO refractory at UTN
 - 2.19 Photo series observed in water experiments: (a) 0sec, (b) 0.25ms, and (c) 0.5ms
 - 2.20 Active sites in stagnant water with different porous refractory
 - 2.21 Active sites in both stagnant and downward-flowing water
 - 2.22 Distribution of argon gas flow velocity in the upper tundish nozzle
 - 2.23 Relation of mean gas flow rate both per unit surface area of UTN wall and per active site in steel caster
 - 2.24 Bubble size distribution with different water velocity and gas flow rate (6.2cm² surface area of refractory sample)
 - 2.25 Comparison of bubble size between measurements and predictions in water model experiment
 - 2.26 Prediction of bubble size in steel caster
 - 2.27 (a) Rosin-Rammler distribution of bubble diameters and number of bubbles and (b) corresponding mass fractions for 9SLPM
 - 2.28 Contact angle (a) before surface coating, (b) after surface coating
 - 2.29 Elemental analysis showing the evidence of surface coating
 - 2.30 Comparison of active sites with and without surface coating of porous refractory in downward-flowing water
 - 3.1 Schematic of the nozzle geometry with slide gate used in Gwangwang Works, POSCO
 - 3.2 Nozzle mesh at different sections with slide gate
 - 3.3 Velocity magnitude distribution in the nozzle with different gas flow: (a) 5SLPM, (b) 9SLPM and (c) 11SLPM (IR: Inner radius, OR: Outer radius)
 - 3.4 Bubble concentration in the nozzle: (a) 5SLPM, (b) 9SLPM and (c) 11SLPM
 - 3.5 Velocity magnitude contour at right nozzle port: (a) 5SLPM, (b) 9SLPM and (c) 11SLPM
 - 3.6 Bubble concentration contour at right nozzle port: (a) 5SLPM, (b) 9SLPM and (c) 11SLPM
 - 3.7 Big bubble formation in recirculation flow
 - 3.8 Half mold mesh without shell
 - 3.9 Velocity vector profile at 50sec after argon gas injection with 5SLPM:(a) top surface (b) center plane between wide faces and (c) narrow face
 - 3.10 Velocity vector profile at 50sec after argon gas injection with 9SLPM:(a) top surface (b) center plane between wide faces and (c) narrow face
 - 3.11 Velocity vector profile at 50sec after argon gas injection with 11SLPM:(a) top surface,(b) center plane between wide faces and (c) narrow face
 - 3.12 Velocity magnitude profiles with different view at 50sec after argon gas injection: (a) 5SLPM, (b) 9SLPM and (c) 11SLPM
 - 3.13 Bubble concentration in half mold at 50sec after gas injection: (a) 5SLPM, (b) 9SLPM and (c) 11SLPM
 - 3.14 Three dimensional view of bubble concentration contours at 50sec after argon

- gas injection with 5SLPM
- 3.15 Three dimensional view of bubble concentration contours at 50sec after argon gas injection with 9SLPM
- 3.16 Three dimensional view of bubble concentration contours at 50sec after argon gas injection with 11SLPM
- 3.17 Cross-flow velocity effect on capture of particle

List of Tables

- 2.1 Casting conditions of slab samples for nail board dip tests
- 2.2 Casting conditions for subsurface hook analysis in slab samples
- 2.3 Properties of porous MgO refractory bricks
- 2.4 Relationship of liquid flow rate between water model and steel caster
- 3.1 Simulation conditions and materials properties used in this calculation

CHAPTER 1. Introduction

1.1 Background

Continuous casting is used to solidify over 90 pct of the 1.1 billion tones of steel produced in the world each year.[1] Fluid flow in the continuous casting of steel is turbulent, transient flow through a complex geometry inlet nozzle into the mold cavity, including the transport of argon bubbles and complex shaped inclusion particles through the turbulent liquid. Fluid flow in the mold is controlled by many design parameters and operating conditions. Nozzle geometry is the most important and includes the bore size, port angle, port opening size, nozzle wall thickness, port shape (round, oval, square), number of ports (bifurcated or multiport), and nozzle bottom design. The flow pattern also depends on parameters that generally cannot be adjusted to accommodate the flow pattern, such as the position of the flow control mechanism (slide gate or stopper rod), nozzle clogging, casting speed, strand width and strand thickness.

Fortunately, other parameters besides nozzle geometry can be adjusted to maintain an optimal flow pattern. These include the injection of argon gas, the submerged entry nozzle (SEN) submergence depth (distance from top of the nozzle port to the mold top surface) and the application of electromagnetic field strengths. In choosing optimal settings for these parameters, it is important to understand how they act together to determine the flow characteristics. An increasing in casting speed, for example, might be compensated by a simultaneous increase in SEN submergence depth (or electromagnetic field strength), in order to maintain the same surface flow velocity. Thus, all the flow control parameters must be optimized together as a system.

In designing the flow system, it is important to consider transients. Sudden

changes are the main cause of the flow instabilities that generate surface turbulence and other problems. Because flow parameters are more easily optimized only for steady operation, each of the parameters that affect fluid flow must be carefully controlled. It is especially important to keep nearly constant the liquid steel level in the mold, powder feeding rate (to keep a constant liquid slag layer thickness), casting speed, gas injection rate, slide gate opening ratio, and nozzle position (alignment and submergence). It is also important to choose flow conditions that are resistant to transients and their detrimental effects, although this is difficult to predict.

A schematic of the continuous casting process is given in Figure 1.1[2], which illustrates some of the phenomena that lead to defects due to fluid flow in the mold region of the process. Jets of molten steel are directed into the liquid through the nozzle ports and traverse across the mold cavity to impinge on the solidifying steel shell near the narrow faces. Gas bubbles in the jet provide lift due to the lower density, which may alter the flow pattern.[3] The jets impinging against the narrow face may cause shell thinning, and even breakouts, if the superheat is too high and the interfacial gap is excessive.

The momentum of the upward flow along the narrow faces can raise the meniscus level there, causing a nonlinear profile along the top surface.[4, 5] Where this level is too high, the infiltration of liquid mold flux into the interfacial gap becomes more difficult, which can lead to nonuniform meniscus heat flux. Excessive surface turbulence may cause rapid fluctuations of the surface level. This can disrupt stable solidification at the meniscus, leading to deep oscillation marks (OMs), surface depressions[6], longitudinal cracks[7] and other surface defects.[8] In addition, high-speed flow across the top surface may shear droplets of liquid mold slag inclusions[9] into the flow, where they may become entrained in the liquid steel leading to skin delaminations, slivers, and other defects in rolled sheet product.[10]

On the other hand, if the surface velocities are insufficient, or if the local superheat contained in the molten steel near the meniscus is too low, then the meniscus may partially freeze to form deep oscillation marks and meniscus hooks as shown in Figure 1.2.[11] This hook is detrimental because they may entrap the mold flux[12] and inclusion-laden gas bubbles[13] into the solidifying meniscus. Hook formation is greatly affected by steel grade, superheat, level fluctuations and oscillation conditions. [14, 15] Superheat also affects the nucleation and growth of equiaxed grains, which controls the solidification structure, and defects such as centerline segregation. The transport of solute with the fluid is also of crucial importance to macrosegregation problems, especially toward the final solidification point lower in the strand.

In addition to molten steel transportation, the jets carry bubbles and inclusion particles into the mold cavity. If the flow pattern enables the particles to reach the top surface, they should be harmlessly removed into the liquid slag layer, so long as the slag is not saturated and the surface tension forces are not excessive. Alternatively, inclusions and bubbles may become entrapped in the solidifying steel shell[16], where they cause slivers, blisters and other costly defects[10] as shown in Figure 1.3.[17] High frequency of entrapped bubble distribution in slabs appears not only in the slab surface region[17] less than 5mm from slab surface even though the sulfur content affects the distribution[18], but also in the internal region[19] more than 25mm from slab surface as shown in Figure 1.4. Inclusion particle behavior is complicated by their attachment to the surface of bubbles, which encourages removal, but also creates potentially dangerous large clusters, which may also be created through collisions.

Many quality problems that originate during the continuous casting of steel, which are above mentioned, can be directly attributed to poor control of fluid flow

conditions in the mold. In order to optimize these flow design and operation conditions, it is crucially important to understand how defects arise and how were changed in the flow pattern affects those defects.

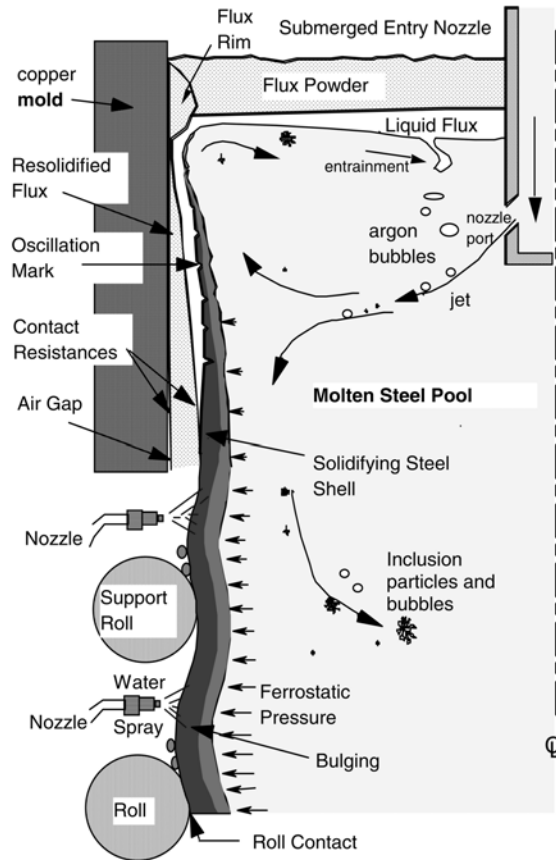


Figure 1.1 Schematic of phenomena in the mold region of a steel slab caster[2]

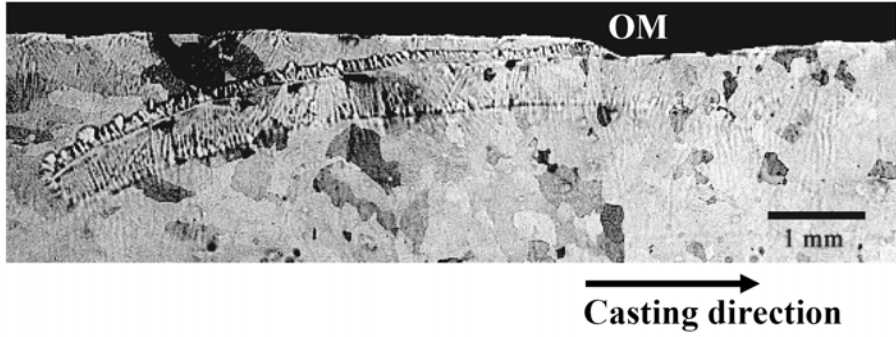
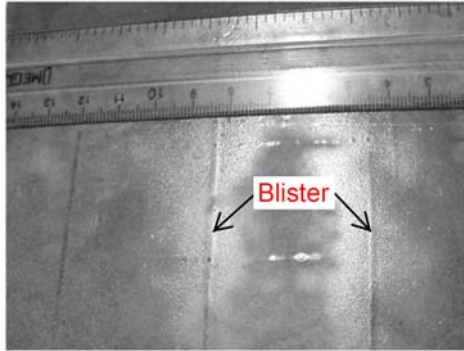
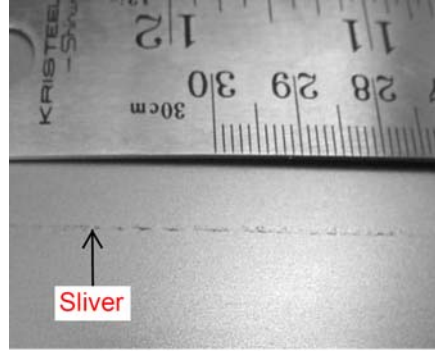


Figure 1.2 Typical curved hook shape[11]

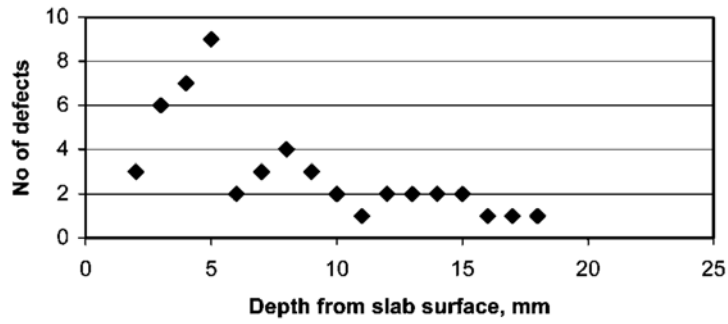


(a)

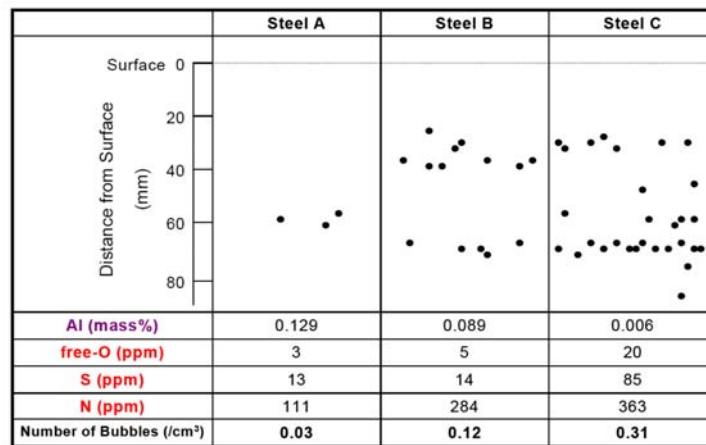


(b)

Figure 1.3 Surface defects due to entrapment of bubble and inclusions resulting in (a) blister, and (b) sliver[17]



(a)



(b)

Figure 1.4 Wide variations of entrapped bubble in slabs: (a) subsurface region[17, 18], and (b) internal region[19]

1.2 Objective of this study

Wide variation of entrapped bubbles in slabs has strong relationship with fluid flow in the mold. To investigate the bubble formation related to fluid flow in the mold, the metallurgical analysis will revealed the locations of entrapped particles in slabs with a careful analysis of samples. And then, two-phase water model experiments will be carried out to measure the initial bubble formation and its behavior in the nozzle. Because the fluid flows phenomena in the real mold cannot be observed directly due to the high temperature of molten steel. From the water model experiments, the bubble size will measured and bubble size in steel caster will predicted using previous bubble size prediction model. These results will used for the multi-phase computational modeling simulation as an input data. A computational modeling will predict the transportation of fluid flow and bubble in the nozzle and mold, and then the results will be verified with observations that have been obtained with the results of the plant experiments.

1.3 Methodology for this study

Wide variation of entrapped bubbles in slabs has strong relationship with fluid flow in the mold. To investigate the bubble formation related to fluid flow in the mold, the metallurgical analysis will revealed the locations of

In order to increase the understanding of the fluid flow and particle transportation phenomena in the nozzle and the mold, three different approaches need to conduct and analysis the fluid flow phenomena in continuous casting process.

- 1) Plant experiments (Metallurgical analysis): The nail board dip tests were conducted to during time periods of steady casting to measure the surface flow phenomena including mold slag thickness, flow intensity,

flow direction, and steel surface profile in the mold with different argon gas flow rates injected into the upper tundish nozzle (UTN) during casting. In addition to nail board dip tests, the investigation of hook near OMs in continuously-cast slab is an evidence to interpret the subsurface defect, because hook forms below \sim mm from the slab surface. This metallurgical analysis is including two-dimensional and three-dimensional analysis collected the samples of ultra-low carbon steel slabs. The samples, matched with nail board dip tests of ultra-low carbon steel slab, were then collected and measured ultrasonically to investigate the internal entrapped defects deducted from the inclusion distribution with distance from the surface of slab samples.

- 2) Physical water model experiments: Due to the high operating temperature, it is difficult and expensive to directly conduct flow measurements in continuous steel casters in order to validate computational model predictions.[20] The physical water model experiments with transparent plastic walls, however, can be used to study single-phase flow in steel casting processes[3, 21-25] where Froude dimensionless number similarity is usually employed, due to the nearly equal kinematic viscosities of molten steel and water. The physical water model experiments were performed to investigate the gas bubble size and its size distribution were measured in specially-treated samples of porous nozzle refractory, and applied to improve the prediction of argon bubble size in steel casters.
- 3) Computational modeling: Computational models have been widely used to simulate multiphase turbulent flow of molten steel. One important phenomenon is the effect of the pressure distribution, buoyancy,

direction, and pattern of the fluid flow, in both the nozzle[26-28] and the mold.[3, 29, 30] Two phase computations of fluid flow and bubble transport in the nozzle and mold were performed, including the effects of slide-gate asymmetry and the predicted argon bubble size distributions based on the physical water model experiment.

The transportation of bubbles and inclusions will be modeled with fluid flow of multiphase computations, and then verified with the trends that have been observed with results of the plant measurements. These results can contribute to increase the interpretation of fluid flow phenomena related to defects in the nozzle and the mold.

CHAPTER 2. Experimental

2.1 Plant measurements

Plant experiments were performed on #2-1 conventional slab caster at POSCO, Gwangyang Works, South Korea, which features a conventional parallel-mold, standard two-port submerged entry nozzle, a 230 and 250-mm thick parallel mold with a fully-adjustable, non-sinusoidal hydraulic mold oscillator and electromagnetic brake ruler system.

2.1.1 Nail board dip test

A. Experimental procedure

The nail board dip test is a useful method to characterizing the flow pattern across the top surface of the mold including the steel surface profile[31], flow intensity, flow direction, and flow velocity, as proposed by McDavid[32] and Thomas.[33] In addition to surface flow pattern, this test can also be indicated mold slag layer thickness. The tests were performed by inserting a row of ~12 stainless steel nails and aluminum wires into a long board as shown in Figure 2.1(a), and dipping them perpendicular into the top surface of the mold along the center plane between the wide faces for 3~4s. After removal, a skull of steel has solidified on the end of each stainless steel nail. The local thickness of the slag layer is indicated by distance from the steel lump to the aluminum wire, which melts back due to its low melting temperatures[31] as shown in Figure 2.1(b). The skull (or knob) profile of all stainless steel nails as shown in Figure 2.1(c) indicates the shape of the steel meniscus. The direction of meniscus flow can be found by recognizing that the high end of each angled skull represents the direction from which steel flow impinges on the nail. The height difference between the low and high ends of the skull profile indicates the magnitude of the local surface velocity as confirmed by Rietow and Thomas.[34]

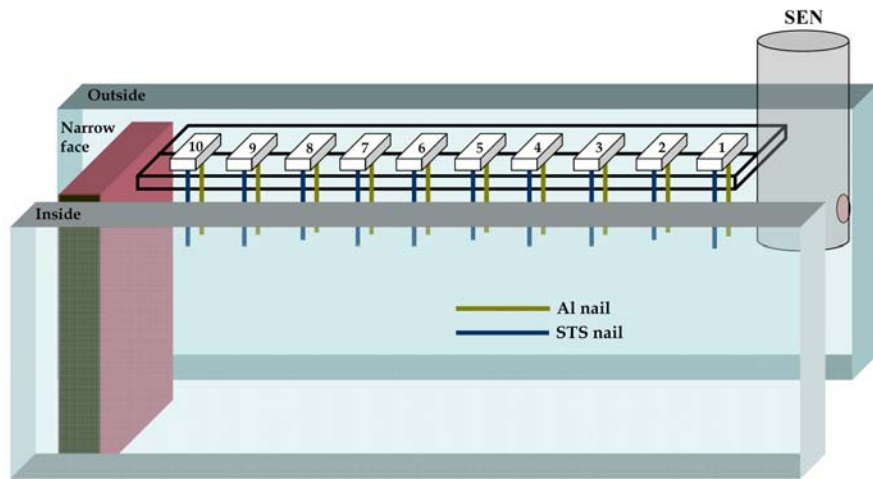
Nail board dip tests were conducted during time periods of steady casting to measure the surface flow pattern with different argon gas flow rates injected into the UTN during casting. The slab width was changed from 1570mm to 1450mm after Test 2. Table 2.1 summarizes the casting conditions.

B. Results

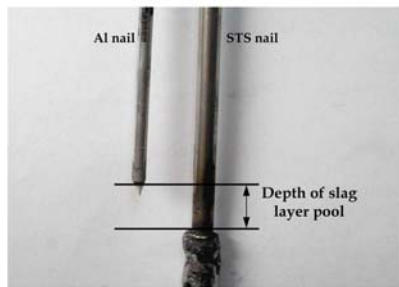
Figure 2.2 shows the meniscus profiles, velocities, and flow directions from all 4 test conditions, according to increasing gas flow rate injected into the UTN, from the nail board dip test analysis. The flow pattern is inferred from the surface profile and flow directions. It appears to change the direction from double-roll pattern, which is generally directed from the narrow face toward the SEN, to single-roll pattern which is generally directed from the SEN toward the narrow face, with increasing gas flow rate. The flow intensity is higher near the narrow face with lower gas flow rate, owing to the upward flow along the narrow face after impingement of the jet stream from across the mold as shown in Figure 2.2(a) and (b). With higher gas flow rate in Figure 2.2(c) and (d), higher flow intensity is observed near the SEN and center region, due to the uplifting buoyancy force of the bubbles on the flow at those regions. The flow direction across the top surface is asymmetrical flow which is mainly directed from the outside radius towards the inside radius at higher gas flow rates.

Table 2.1 Casting conditions of slab samples for nail board dip tests

Test number	Slab thickness (mm)	Pour temperature (°C)	Electromagnetic current (A)	Slab width (mm)	Casting speed (m/min)	Argon gas flow rate (SLPM)
Test 1	250	1567	250	1570	1.30	9.60
Test 2						12.20
Test 3				1450	1.34	6.18
Test 4						4.58



(a)

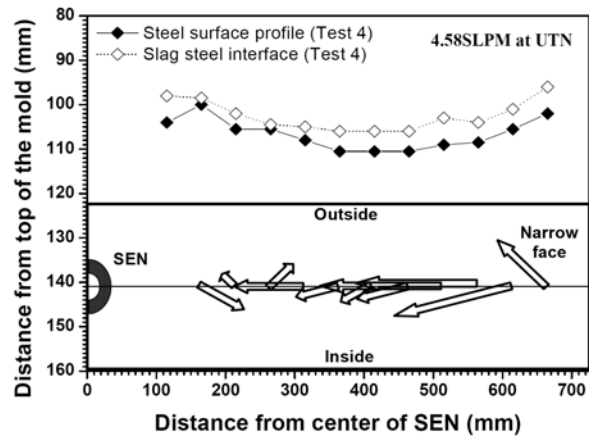


(b)

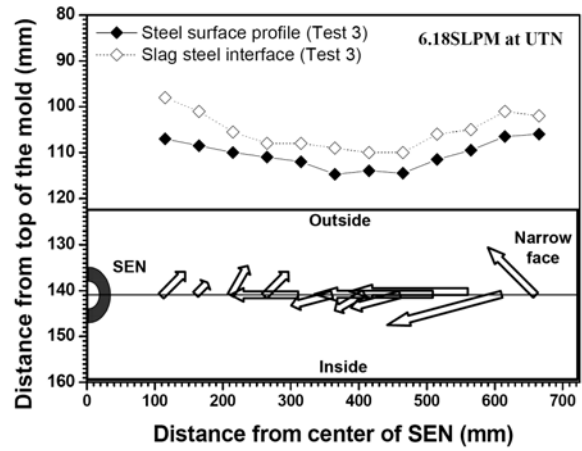


(c)

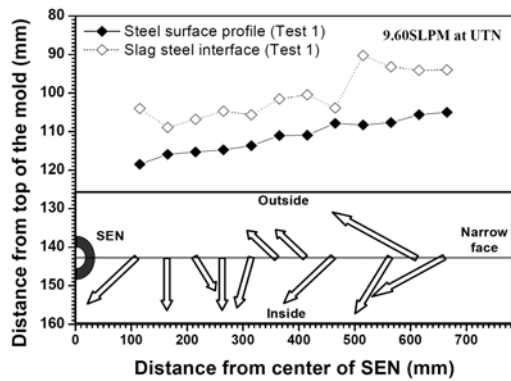
Figure 2.1 (a) Schematic diagram of nail board, (b) an example of aluminum and stainless steel nails and (c) close view of the stainless steel nail showing solidified lump, which reveal surface velocity



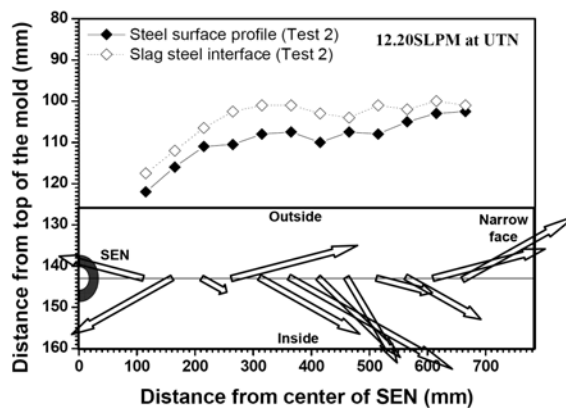
(a)



(b)



(c)



(d)

Figure 2.2 Measured mold slag layer thickness, steel meniscus profile, and surface flow direction according to the gas volume fraction at UTN: (a) 3.63%, (b) 4.84%, (c) 7.00%, and (d) 8.73%

2.1.2 Particle entrapment near subsurface hook region in slabs

A. Introduction

Deep oscillation marks[35] and subsurface hooks[36] in continuously-cast steel slabs are associated with many slab quality problems. Specifically they tend to entrap argon bubbles and alumina inclusions near the hooks[37, 38], leading to slivers and blisters, and transverse cracks often form near the roots of deep OMs.[39-41] In extreme cases, the entire slab surface must be ground or “scarfed” to remove all traces of the hook microstructure, resulting in high cost and loss of productivity.[42] OMs are periodic depressions or grooves in the strand surface that run around the perimeter of continuous-cast steel. Subsurface hooks are distinctive micro-structural features which extend from some oscillation marks and can be identified by etching transverse sections near the slab surface.[35, 36, 40]

Hooks and OMs form due to many interdependent, transient phenomena that occur simultaneously during initial solidification near the meniscus in the mold. Several different mechanisms have been proposed in previous literature. J. Sengupta *et al.*[43, 44] have recently suggested a new mechanism for hook and OM formation, which is illustrated in Figure 2.3. Hooks form in ultra-low carbon (ULC) steel grades are reported to be particularly prone to hook formation[45], perhaps owing to their thin mushy zone, and formed by periodic meniscus solidification and subsequent liquid steel overflow and OMs form by normal steel shell growth before and after the overflow. This mechanism was based on a careful analysis of numerous specially-etched samples from ULC steel slabs in controlled plant trials[14, 15] at POSCO Gwangyang Works. Furthermore, this analysis explains observations in previous literature, theoretical modeling results[43], and is supported by microstructural evidence obtained using[44] both optical microscopy and microanalysis techniques.

The present study was conducted to reveal the complex 3-D shape of the frozen meniscus hooks and OMs near the slab corners. Samples of ultra-low carbon steel were studied because these grades ($C \leq 0.05\%$) are particularly prone to both OM and hook defects. A variety of cross sections near the slab corners were specially etched and analyzed to distinguish the frozen meniscus shape, including vertical, horizontal, and angle sections at different depths and locations in three slab samples taken from the slab corners. The results provide unique evidence of sub-surface micro-structural evolution in the meniscus region near the slab corners of continuous-cast steel.

B. Experimental procedure

Samples from the slab corners of 230 X 1300mm ultra-low carbon steel slabs were obtained from plant experiments performed on #2-1 conventional slab caster at POSCO, Gwangyang Works, South Korea. The casting speed was kept relatively constant at 1.45m/min. Table 2.2 summarizes the casting conditions employed during casting of the slabs that contained the samples for the subsurface hook region. The casting conditions of samples I, II, and III match the conditions of Tests 10, 3 and 9 in reference[14] respectively. Further details of these plant experiments, including the composition of the ultralow-carbon steel grade and mold powder is given in reference[14].

Sample I (10mm wide x 20mm deep x 20mm long) encompassed 2 OMs and was obtained near the corner, as shown in Figure 2.4(a). Horizontal sections were cut through the tip of the oscillation marks at the corner at 0.3mm, 0.8mm, and 1.0mm locations above the OM tip, as shown in Figure 2.4(b), Optical micrographs are presented for the 1st oscillation mark.

Sample II (13mm wide x 20mm deep x 30mm long) encompassed 4 OMs and was obtained near the corner of a different slab, as shown in Figure 2.5(a). Vertical sections through this sample were taken at various distances (0.7 to

~5.5mm) from the wide face surface, by polishing, etching, photographing, and then regrinding at intervals of about 0.5mm, as shown in Figure 2.5(b). These sections parallel to the wide face revealed characteristic subsurface micro-structural features, which were interpreted by extracting hook shapes to construct the 3-D hook shape. Further vertical sections were taken at 20mm, 75mm and 115mm (center line) from the slab corner from the same slab and hook depths and shapes were measured from micrographs of each section.

Sample III (100mm long and encompassing 9 OMs) was obtained near the corner from a different slab and was divided into three pieces each about 30mm long, as shown in Figure 2.6(a). Each sample was then cut at a different vertical orientation to reveal the subsurface microstructures, as shown in Figure 2.6(b) through (d).

Further slab samples were taken for other conditions (Heats 4 and 5[15] in Table 2.2) and hook depths were measured from vertical sections taken from each sample around the perimeter of the narrow face (5 locations) and wide face (7 locations).

All of the sections were ground, polished, and then etched by a special etching method[43] to reveal the microstructure and hook shapes in ultra-low carbon steel samples. The etching reagent was picric acid solution (2,4,6-trinitrophenol) with additions of surfactant zephiramine (benzyltrimethyl-n-tetradecylammonium chloride) and etched for ~1-1.5 h. Further details are given elsewhere.[43]

C. Results

Oscillation marks are well known to “point” downwards at the corners, indicating the casting direction, as shown in Figure 2.4(a). The lowest point of each oscillation mark is found at the corner, extending 2-3mm below the average around the perimeter, as shown in Figure 2.5(b). The reason for this is

clarified by analysis of the horizontal section micrographs of Sample I in Figures 2.4 and 2.7, which also reveal new insights into hook formation in the slab corner.

Each micrograph in Figure 2.7 exhibits two distinct layers of frozen steel at the corner, which formed at different times. The schematic in Figure 2.4(b), explains the appearance of these microstructural features. After the 3-D meniscus in the corner freezes to form the hook, it shrinks to pull away from the mold walls. Liquid steel overflows the solidified meniscus, as pictured in Figure 2.3(b), and then flows down into the corner gap between the hook and the mold. It can flow further downward in the corner region, owing to the shrinkage gap there. As the overflowing liquid freezes, its horizontal cross section naturally decreases, ultimately ending in a tip, which forms the point of the OM tip at the corner. A small thin layer, which is outlined with a solid red line in Figure 2.7, is seen on the surface at the corner clearly shows evidence of this phenomenon. The area of this outlined solid red line decreases in size with decreasing vertical distance to the OM point (i.e. from 1.0 to 0.8 to 0.3mm). These areas slice through the base of the hook, which was originally the frozen meniscus. Furthermore, the enlarged inset in Figure 2.7(c) clearly shows valleys on each side of this surface layer, which represent the vertical component of the steep-sloping OMs near the corners, observed in Figure 2.4(a). The distinct microstructure of this layer indicates that it formed later, from liquid running down the surface.

The tip of this overflowed region penetrates further into the corner, where the gap between the mold and the frozen meniscus hook is largest. This larger gap also decreases heat transfer in the corner prior to the overflow, leading to less meniscus freezing. This explains why the hook is thinner in the corner, which is seen by following the hook, demarked by the dark thin discontinuous subsurface line, around the corners in Figure 2.7.

Micrographs of vertical sections (Sample II) presented in Figure 2.8 show great differences in hook shapes near the corner. The curved line along the center of each hook represents the “line of origin” of the hook, and indicates the shape of the meniscus when it froze. Solidification then proceeded in both directions away from this line, slowing temporarily when thermal gradients diminished, to leave the dark bands that outline each hook. The lines of hook origin traced from a series of ten such vertical sections are shown in Figure 2.9(a). A true three-dimensional schematic of the hook shape around the slab corner, given in Figure 2.9(b), was constructed from the hook outlines surrounding the 2nd OM in Figure 2.8. The upper lines (blue solid) outline between the frozen meniscus and the liquid that overflowed the frozen meniscus. The lower lines (red dashed) indicate the boundary between the supercooled frozen meniscus and the molten steel pool below. The vertical distance in Figure 2.9 is measured in the casting direction relative to the arbitrary zero-reference height taken midway between the first and second oscillation marks.

Figure 2.10 was constructed to show the top view of the three OM hooks in Figure 2.9(a). This graph clearly reveals the three-dimensional shape of the frozen meniscus and hooks, which extends continuously from the OM perimeter around the slab corner. The 3rd OM hook is consistently smaller than its neighbors. This indicates that changes in meniscus conditions extending around the corner but lasting less than a second are very common. This is likely due to transient fluid-flow phenomena, such as surface level and superheat fluctuations, which vary even under steady casting conditions. Figure 2.10 also explains the observation in Figure 2.8 that the 2nd OM hook is triple the depth of the 3rd OM at 2.5 mm from the corner, but only twice the depth at 3.5mm.

The micrograph in Figure 2.11(a) shows the deepest extent of the hooks,

which is observed in a 45 degree vertical cross section from the corner, as shown in Figure 2.6(c). Figure 2.11(b) shows the approximate 2-D hook shape constructed at different vertical sections through different oscillation marks near the corner. The hooks at the corner start about 0.75mm lower than other two nearby observations. This indicates the downward-pointing OM caused by the furthest penetration of overflowing liquid steel into the flux channel at the corners, as discussed earlier. Narrow-face hooks are slightly deeper than wide-face hooks, owing to the generally lower superheat there, and correspondingly more meniscus freezing. This effect is greatly exaggerated in Figure 2.11(b), due to the proximity of the 2-D sections to the corner. This same reason causes the difference between hook depths in Figure 2.8, and is explained with Figure 2.10. Figure 2.11(b) also shows that corner hooks at the 45 degree plane sometimes exhibit concave curvature. At other locations, hooks are always convex-shaped, and match well with Bikerman's equation, as observed clearly in previous work.[14, 15, 43, 46] This concave curvature at the corner, can not be predicted by the two-dimensional equilibrium meniscus shape of Bikerman's equation, which is determined solely by the balance of surface tension and ferrostatic pressure forces[47, 48]. This observation suggests that other effects, such as three-dimensional, transient pressure variations caused by the moving slag rim attached to the mold wall are more influential near the slab corners than elsewhere. This is consistent with a thicker solidified flux rim in the colder corners.

Figure 2.12 compares hook depths around the perimeter of slab sample II, as shown in Figure 2.5(a). The maximum hook depth appears at the corners, owing to further meniscus solidification, likely due to the colder liquid found in this region. Hook depths[15] measured around the slab perimeter including narrow face and wide faces are shown in Figure 2.13. Hooks extend continuously around the entire slab perimeter, although they are often difficult to etch. The

hooks are always deepest at the corners, by 10 to 100%.

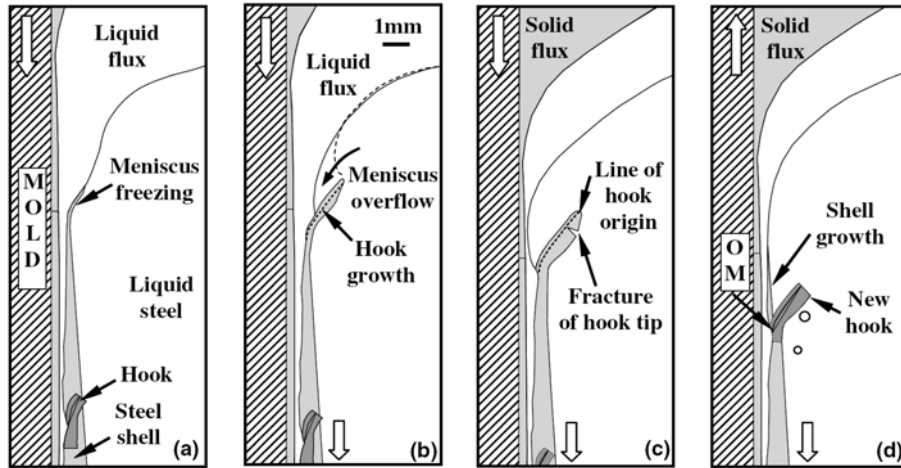
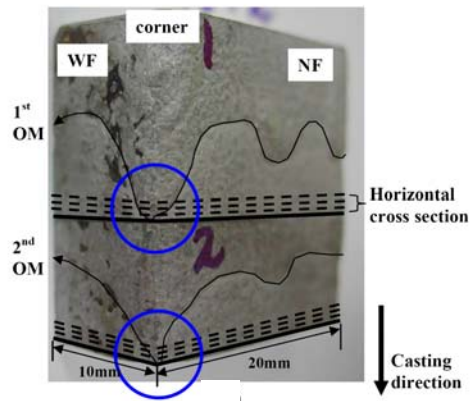


Figure 2.3 Schematic illustrating formation of curved hooks in ULC steel slabs by meniscus solidification and subsequent liquid steel overflow[43,

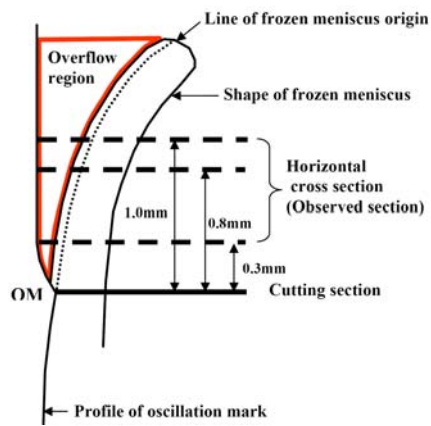
44]

Table 2.2 Casting conditions for subsurface hook analysis in slab samples

Sample number	Casting speed (m/min)	Slab width (mm)	Pour temperature (°C)	Mold oscillation stroke (mm)	Mold oscillation frequency (cpm)	Non-sinusoidal mold oscillation ration (%)	Superheat (°C)	Electro-magnetic current (A)
Sample I			1559	7	145	12	26	
Sample II	1.45	1300	1571	5	174	12	38	300
Sample III			1559	7	124	0	26	
Heat 4	1.47	1570	1571	6.9	159	12	38	277
Heat 5			1567	6.9	160	12	34	0

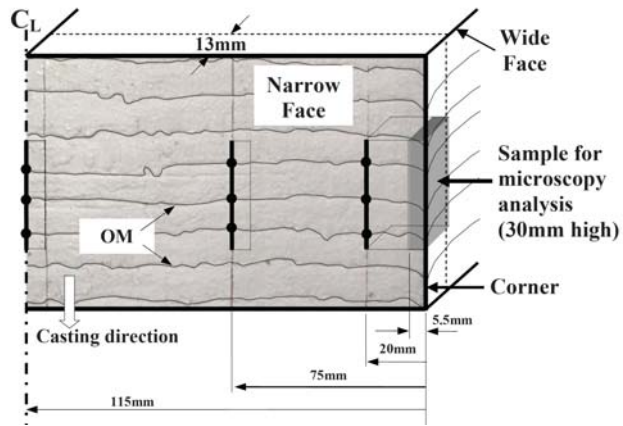


(a)

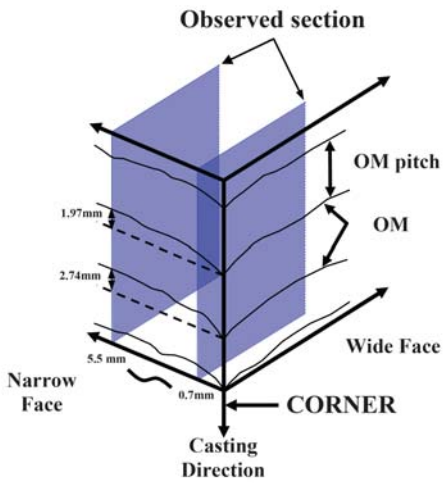


(b)

Figure 2.4 Sample I (a) location obtained from slab corner and (b) three different horizontal sections cut for microscopy analysis of hooks and oscillation mark shown in circles



(a)



(b)

Figure 2.5 Sample II (a) location obtained from slab corners and (b) location of sections cut for microscopy analysis showing oscillation mark shape

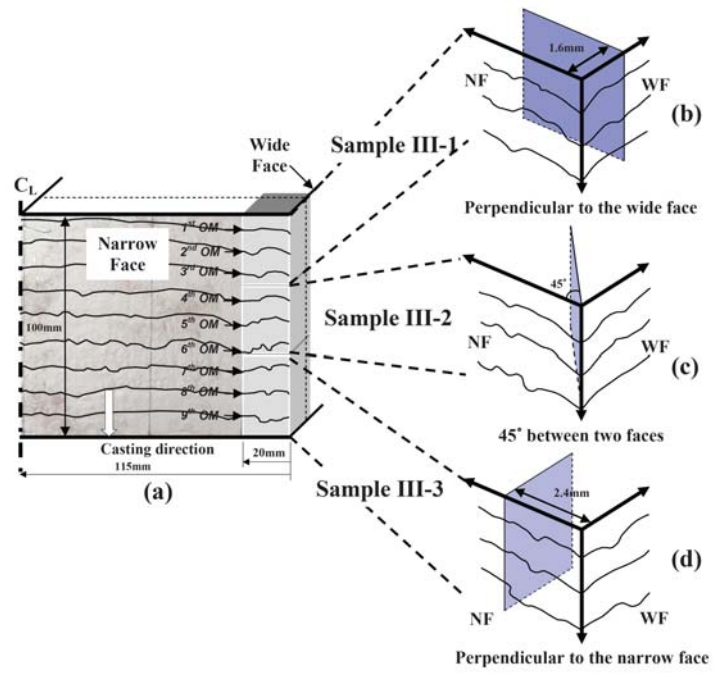


Figure 2.6 Sample III (a) location obtained from slab corners and (b) ~ (d) orientation of three different vertical sections cut for microscopy analysis

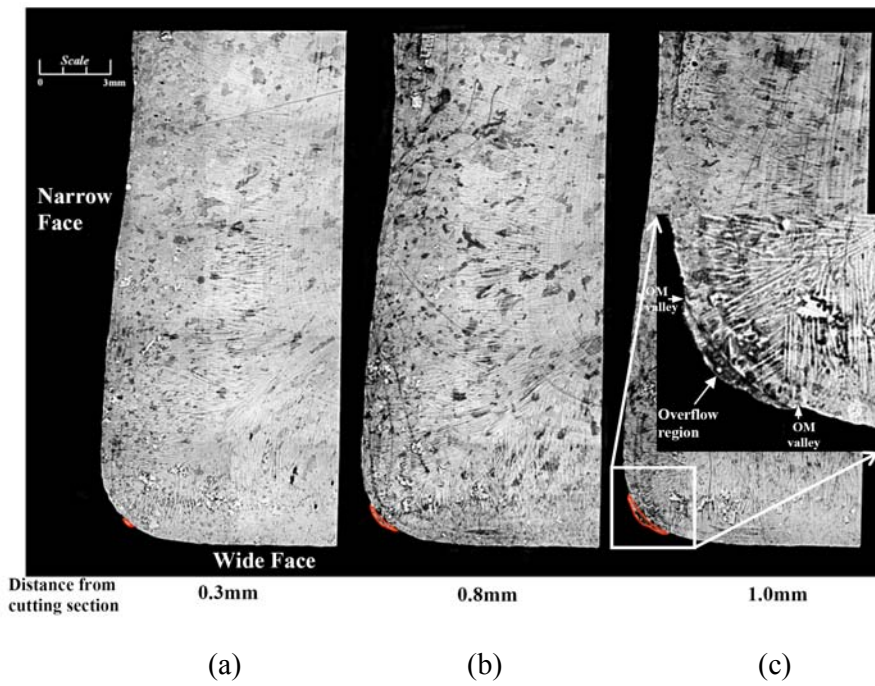


Figure 2.7 Optical micrographs of horizontal cross sections (Sample I) showing evidence of liquid steel overflow

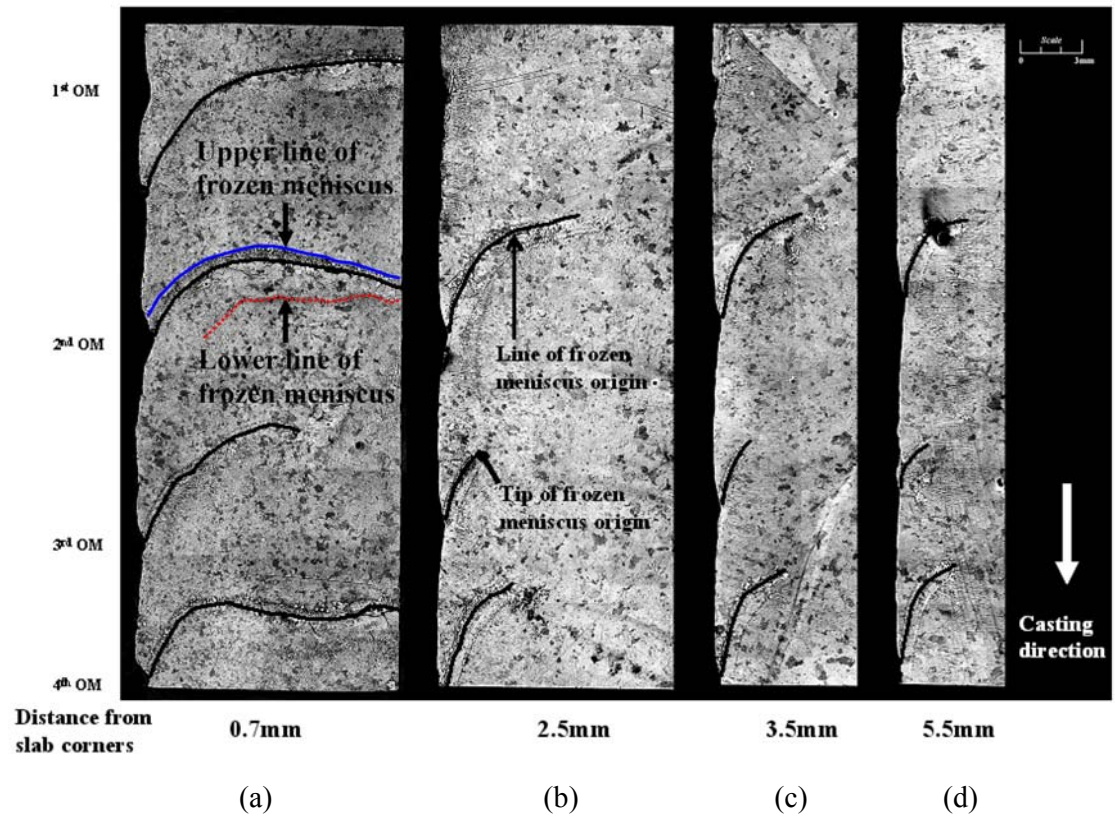
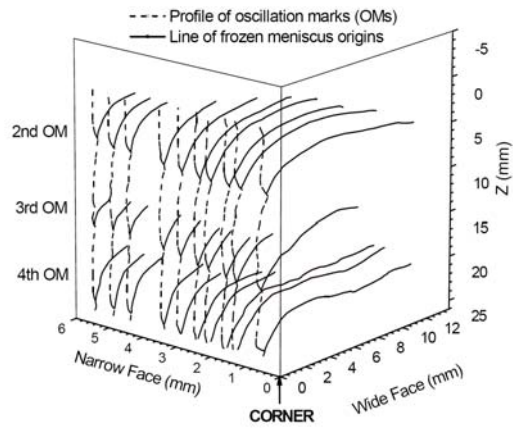
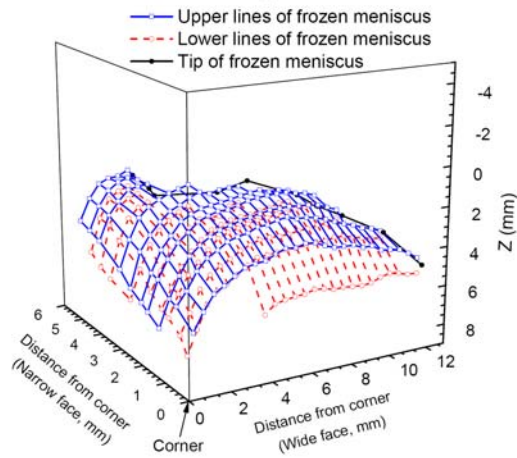


Figure 2.8 Optical micrographs at different distances from wide face (sample II) showing line of frozen meniscus origin: “hooks”



(a)



(b)

Figure 2.9 Line of frozen meniscus origins obtained from micrograph analysis of Sample II (a) and (b) 3-D shape of frozen meniscus hook at 2nd OM

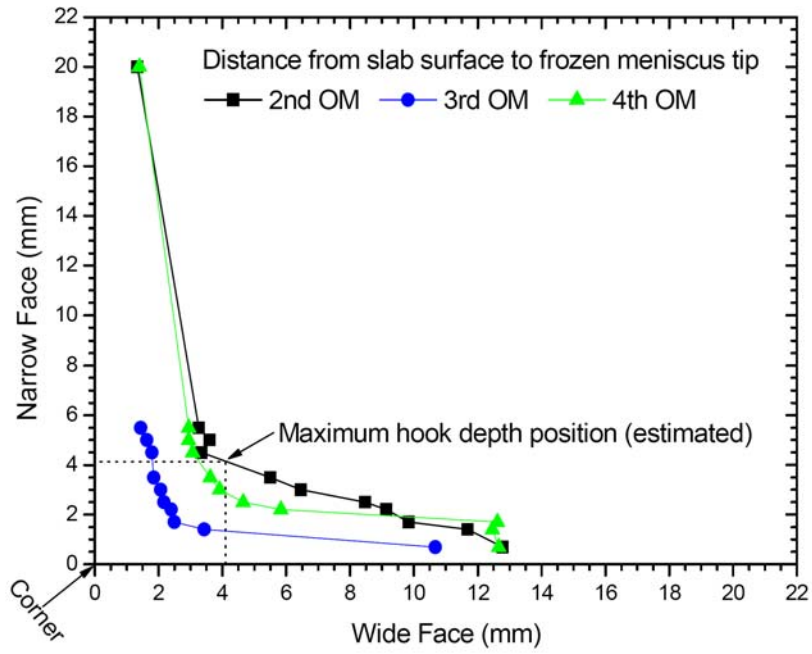


Figure 2.10 Top views of lines of frozen meniscus origins (hooks) from micrographs (Sample II) showing hook depth increase around corner and explanation of hook depth variations observed in micrographs

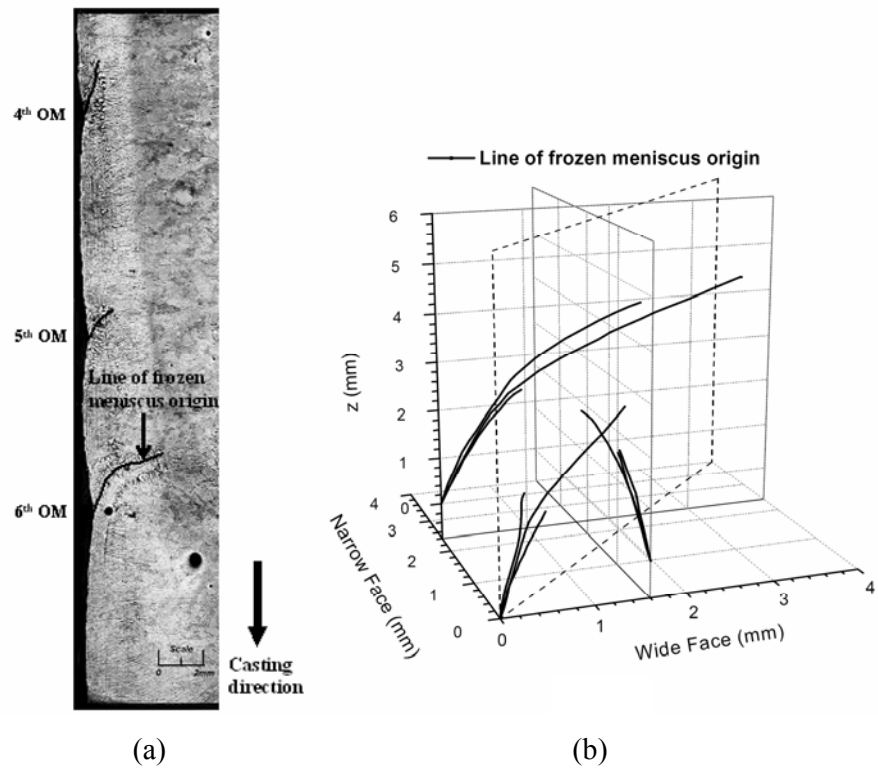


Figure 2.11 Hook shapes (lines of frozen meniscus from vertical sections through sample III) (a) micrograph of 45 degree section and (b) shapes traced from three different hooks

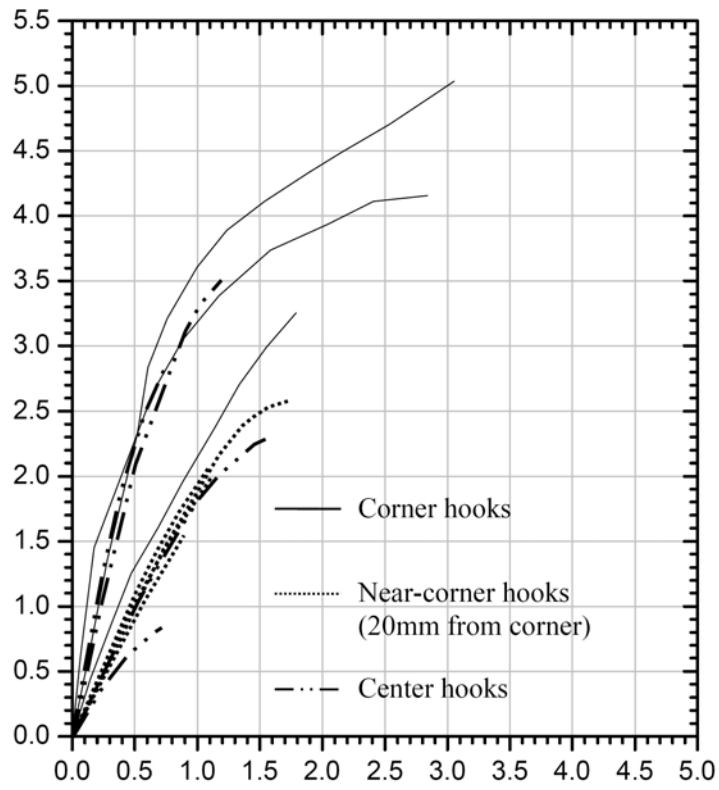
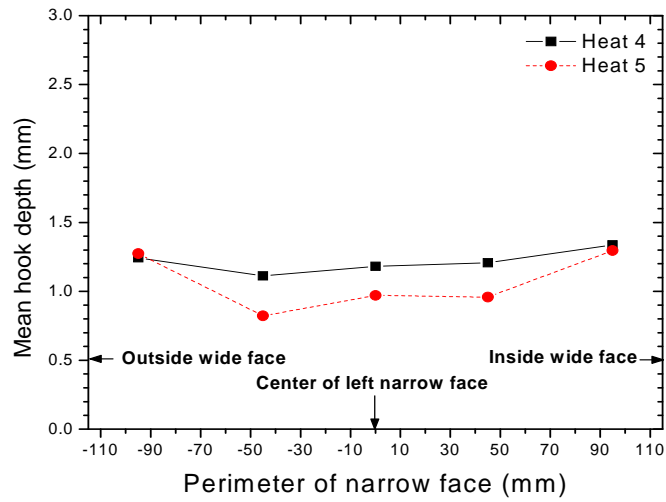
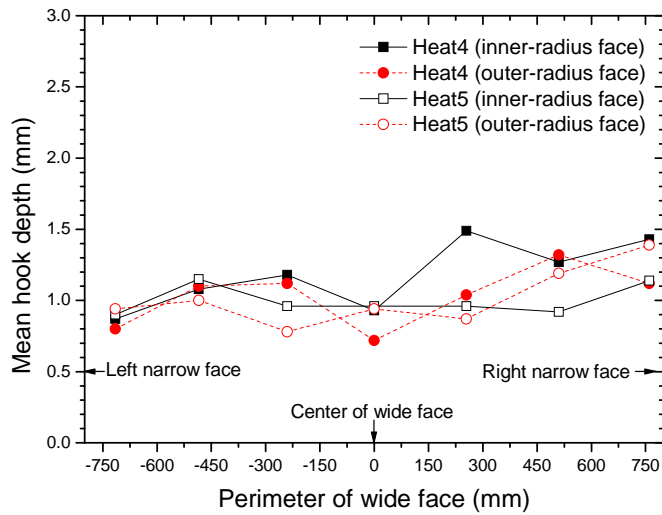


Figure 2.12 Lines of frozen meniscus (sample II) at three locations around slab perimeter of narrow face, showing increase in hook size towards corner



(a)



(b)

Figure 2.13 Hook depth variation along mold perimeter of (a) narrow face and (b) wide face

2.1.3 Particle entrapment in internal region in slabs

A. Introduction

Particles (inclusions and/or bubbles) traveling in the liquid pool may become entrapped into the solidifying shell to form defects. Entrapped solid oxide particles eventually lead to internal defect, which act as stress concentration sites to reduce fatigue and toughness properties of the final product. Gas bubbles captured in this way eventually may cause blister defects such as “pencil pipe” which appear as streaks in the final rolled product.

From the impingement point on the narrow faces in the mold, the jets from nozzle ports split upward and downward, flowing to create an “upper roll” above each jet and a “lower roll” in the lower regions of the strand. These flow pattern in the mold, furthermore, has been shown to depend on both the gas injection rate and the size of argon bubbles.[3, 49] The entrapment locations in the strand are distributed both upstream and downstream. Defects distribution in the continuous slabs were detected and found as a function of depth from slab surface and the entrapment position of defects was various.[17-19]

In this study, slab samples were collected during casting trials conducted at Gwangyang Works, POSCO for changing gas flow rate at UTN. Particle entrapped locations were detected using ultra sonic analysis from sectioned slab samples and correlated with results of nail board dip test.

B. Experimental procedure

The conditions of each slab samples for these measurements were corresponding with the parameters as shown in Table 2.1. Samples were cut along a quarter and center position from narrow face and sections through four samples (100 wide x 60mm deep x 100 long) were cut, ground, and polished from both inside and outside faces, as shown in Figure 2.14(a). Each section was analyzed ultrasonically for all particles including non-metallic inclusions

and/or bubbles larger than $113\mu\text{m}$ captured within 60mm from the slab surface oscillation marks as shown in Figure 2.14(b).

C. Results

Figure 2.15 shows the location of entrapped particles inside the slab samples with casting conditions shown in Table 1. Shell thickness profiles down the caster below the meniscus are calculated using CON1D[15] model simulations for each test shown in Table 1, to show the corresponding distance below the sample surface, as shown in Figure 2.16. The transition from straight to curved regions of the caster occurs at $\sim 3\text{m}$ ($\sim 30\text{mm}$ shell thickness). Previous work has shown the particles trapped by initial solidification hooks occur within just a few mm of the meniscus.[43, 50, 51] The majority of particle entrapment in Figure 2.15 occurs in between these two regions, so must be controlled by a different mechanism. At lower gas flow rate, the defect distribution is similar on the inside and outside radius and big defects were inspected near the subsurface hook region. However, at higher argon gas flow rate, the distribution is very asymmetrical, namely almost all particles are trapped within straight region on the inside radius. Almost none are found on the outside radius. This is likely due to the asymmetric flow towards the inside radius. Thus, gas injection through the nozzle greatly affects both fluid flow in the mold and defect distribution in the slab.

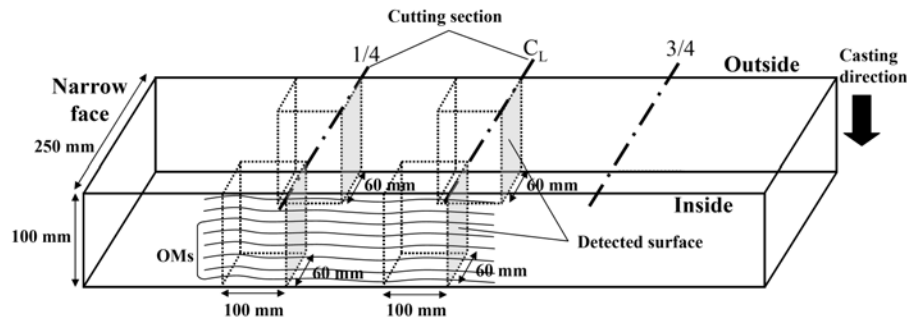
2.1.4 Summary

The 3-D shape of the frozen meniscus, subsurface hook microstructure, and oscillation marks in continuous-cast ultra-low carbon steel slabs has been investigated by analyzing micrographs of carefully-etched samples near the corners. The horizontal sections provide clear evidence that OMs formation due to liquid steel overflow. The line of hook origin in the subsurface

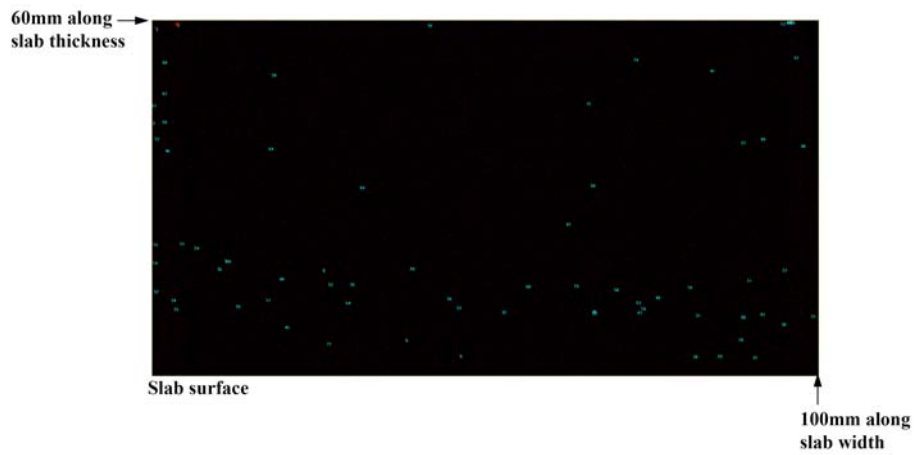
microstructure indicates the original shape of the frozen meniscus. A graphical reconstruction of the 3-D hook shape in the corner from a series of vertical cross sections explains the progression of 2-D hook microstructures observed around the slab perimeter. The classic 2-D hook microstructure simply curves continuously around the corner, increasing in size towards the corner. The shape, size, and depth of this continuous hook structure have been quantified. The 3-D shape of the continuous plane of hook origin matches the expected shape of the frozen meniscus in the corner. Deeper hooks in this region might arise from lower superheat, or higher pressure from the deeper flux rim during mold oscillation expected in the corner. These results confirm the mechanism for the formation of hooks and OMs by meniscus solidification and subsequent liquid steel overflow suggested by J. Sengupta *et al.*[51] Oscillation marks extend further in the casting direction at the corner due to the ease of liquid steel overflow into the larger gap there. These results will provide a foundation for future computational models and plant trials to understand and control hook and OM formation near the slab corners.

The surface flow pattern in the mold is measured and discretized with the nail board dip tests. Increasing gas flow rate at UTN, the flow pattern is changed from double roll to single roll. The direction of surface flow with higher gas flow rate in the mold is an asymmetric flow toward inside wide face. The location of entrapped particles (inclusions and bubbles) in the slab is investigated as a function of distance from the surface of slab sample. Near the slab surface, the hook as a subsurface defect is quantified with various perimeter of slab. The deepest hook, which is related to the surface quality, exists around slab corners is confirmed using metallurgical analysis. The internal defects were detected using ultra-sonic analysis. The distribution of entrapped particles with higher gas flow rate is very asymmetrical. The reason of asymmetric distribution with higher gas flow rate causes from asymmetric

flow between wide faces in the mold, corresponding with results of nail board dip tests.



(a)



(b)

Figure 2.14 (a) Schematic of sample locations and surfaces of particle analysis for each test in Table 2.1, and the result of (b) the signal map using ultrasonic analysis

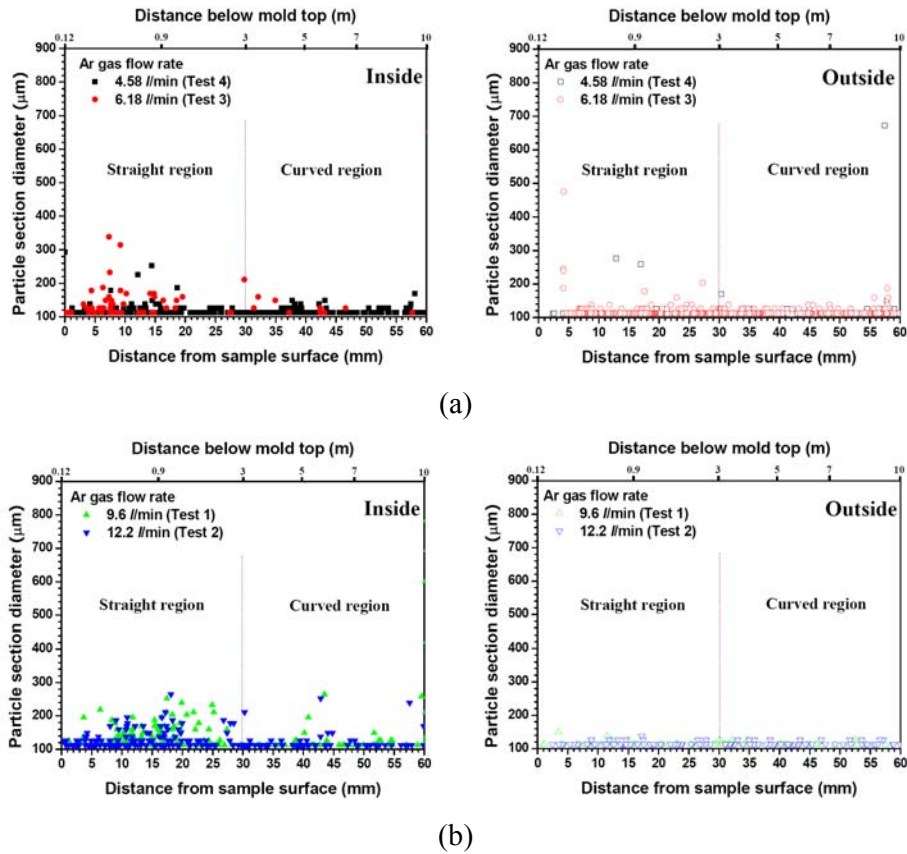


Figure 2.15 Locations of entrapped particles in slab samples with casting conditions shown in Table 1: (a) low gas flow rate, (b) high gas flow rate

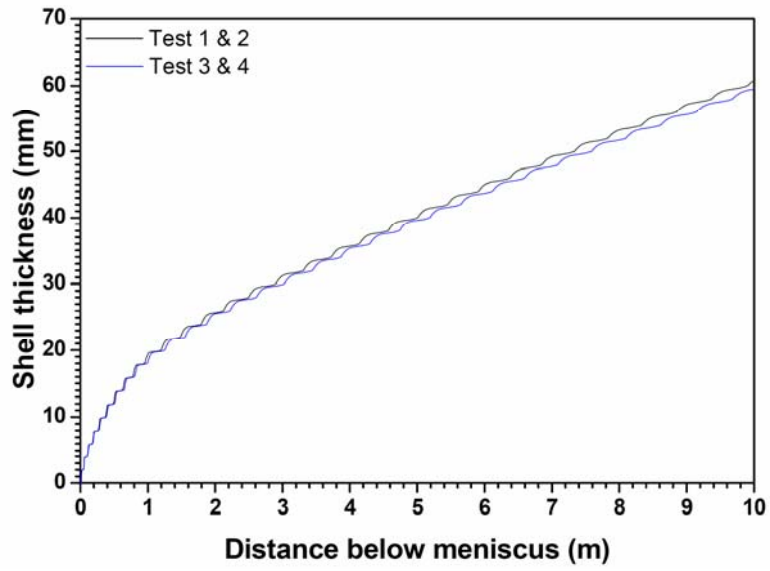


Figure 2.16 Shell thickness prediction in the mold by CON1D[15]

2.2 Water model experiments for initial bubble behavior

2.2.1 Introduction

Extensive studies[52-56] of bubble formation have been done on aqueous systems, both experimentally and theoretically. Recently, Wang *et al.*[57] used water models to study air-bubble formation from gas injected through a porous refractory into an acrylic tube with flowing water. The wettability was reduced by waxing the nozzle walls, which caused the gas to form a large curtain traveling along the wall, which broke into many uneven-sized bubbles. On an unwaxed surface, uniform-sized bubbles formed and detached from the wall to join the liquid flow.

In this study, water model experiments are performed to investigate the initial bubble formation in upper tundish nozzle flow. These include the effect of liquid velocity, gas injection flow rate, and surface contact angle on the bubble size, distribution, and the active sites on porous refractory surface. In addition to quantifying these important parameters, the results of these water model experiments also encourage to the similarity compare to actual plant using the concept of active site and give the input data for two phase computational model of fluid flow later.

2.2.2 Experimental Procedure

Figure 2.17 shows a schematic of the 1/3 scale water model experimental apparatus from tundish to mold, as simulated the caster with slide gate system for control of steel throughput at Gwangyang Works, POSCO. Water is pumped from water bath in the bottom of the mold into the tundish and flows down from the tundish through submerged entry nozzle with injected gas at UTN, and into water bath circulatory. The gas flow controller is adjusted to achieve volumetric gas flow rates of 0.2 ~ 1.0SLPM (standard liter per minute), and the water flow rate is controlled by the open ratio of slide gate system,

which the moving direction is perpendicular to the nozzle port direction. The average water flow rate varies from 20 ~ 45LPM (liter per minute), which corresponding to the average water velocity inside the nozzle from 0.68 to 1.58m/s. The average water flow velocity is obtained from the water flow rate divided by the cross-section area of nozzle bore.

To investigate the formation of bubbles and its behavior in the nozzle after gas injection, the UTN is made as 140mm long transparent acrylic tube with a square 22 x 22mm cross section to keep the cross section area in comparison with 25mm diameter cylindrical SEN. The square shape of upper tundish nozzle is useful to observe the initial bubble behavior inside the nozzle without reflection of bubbles. The brick pieces of MgO porous refractory (14mm wide x 44mm long x 17mm deep) were made to simulate the actual dolomite refractory with different properties, as given in Table 2.3 and inserted into the center position of upper tundish nozzle to simulate the actual porous dolomite refractory, as shown in Figure 2.18. The gas is spread out in the gap between the porous refractory and the acrylic cap, and injected by pores on inner wall surface through a lot of connected pores inside porous MgO refractory. The initial behavior of injected bubbles before entering slide gate is recorded by a high speed camera with 4000 frames per second, and then studied by inspecting the video images frame by frame, as shown in the representative recorded images of Figure 2.19 with different water flow rate and gas flow rate.

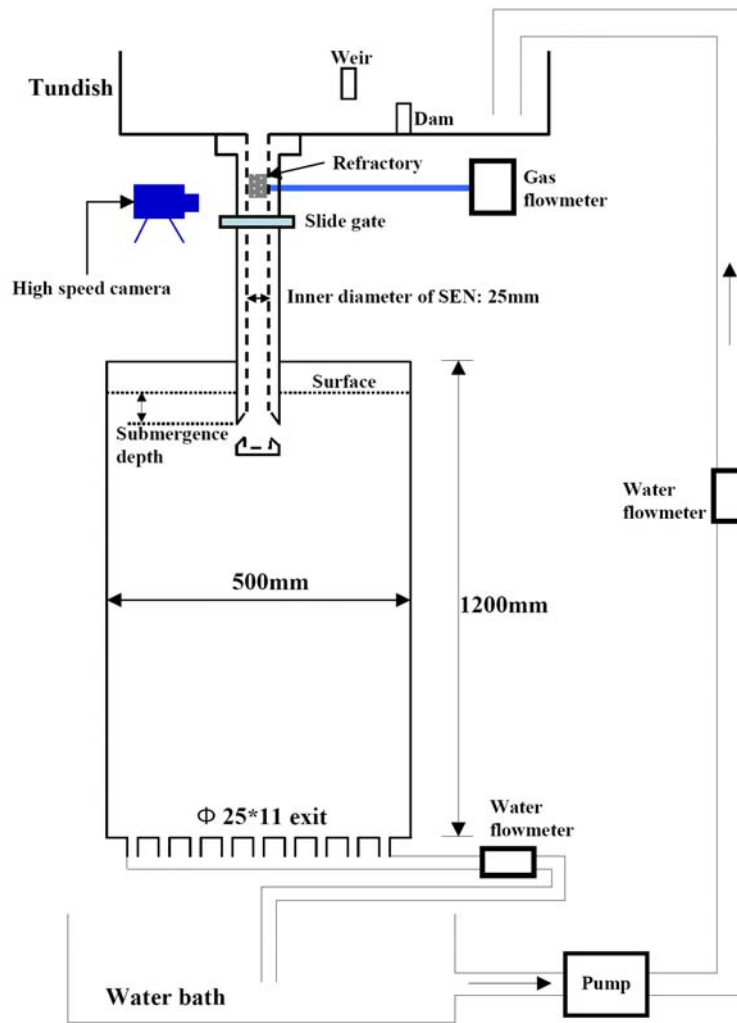


Figure 2.17 Schematic of 1/3 water model experiment

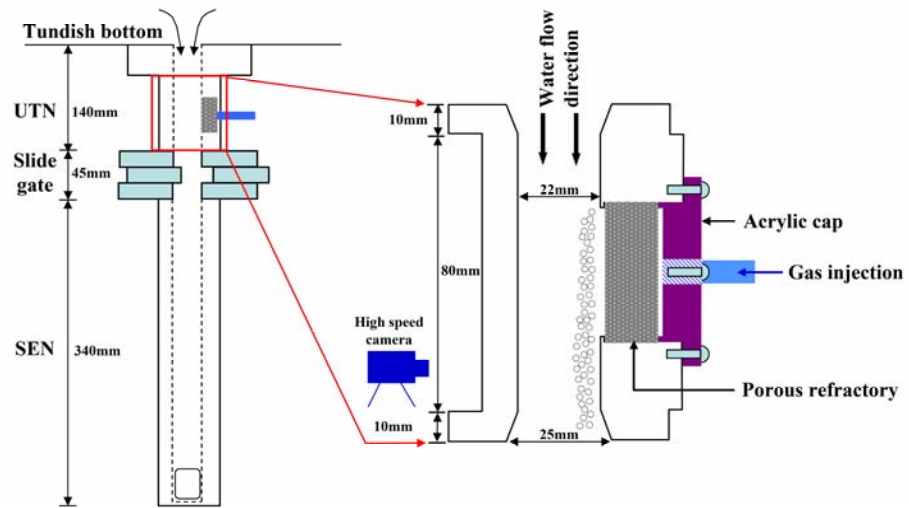


Figure 2.18 Gas injection through porous MgO refractory at UTN

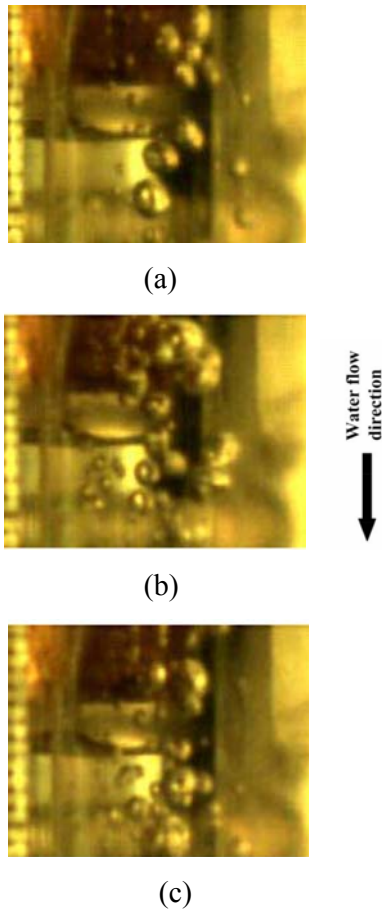


Figure 2.19 Photo series observed in water experiments:
(a) 28.2LPM & 0.1SLPM, (b) 28.2LPM & 0.3SLPM, and (c) 36.8LPM &
0.3SLPM with 7.52nDm permeability

Table 2.3 Properties of porous MgO refractory bricks[58]

	Brick 1	Brick 2	Brick 3
Fired B. D. (g/cc)	2.9	2.9	2.8
Porosity (%)	16.2	17.6	17.6
Modulus of rupture (psi)	1085	1119	1467
Average pore perimeter (um)	252	302	306
Average pore area (um ²)	3097	4928	4949
Permeability (nPm)	7.52	16.32	26.12

2.3.3 Active sites measurements on refractory surface

In this work, the active site which indicates the actual site exiting bubble on the inner surface of porous refractory was used for the effect of refractory properties on the initial bubble behavior.

A. Stagnant flow

Although most of previous studies are based on bubble formation from an upward-facing orifice or nozzle, some authors[55, 59] observed that bubbles formed from a horizontal orifice behaved almost the same as in stagnant liquid. In this study, experiments are first performed simply in stagnant water by immersing the UTN into the water bath using a porous refractory. Figure 2.20 shows the measured active sites with different permeabilities of porous refractory.

It can be seen that active sites increase with increasing gas injection flow rate. For the same gas injection flow rate, a higher permeability of porous refractory makes less active sites. This suggests that the permeability has an effect on to determine the bubble formation in the nozzle.

B. Downward flowing

Experiments are next performed with gas injection through the porous refractory without surface coating into downward flowing water. For the water flow rate in water model experiment was determined by matching the flow velocity in the nozzle on both systems, because the properties of porous refractory such the pore size was not scaled according to the water model scale. In this way, the casting speed will be obtained by mass balance law, like as below.

$$Q_w = U_w \cdot A_w \quad \therefore U_w = \frac{Q_w}{A_w} \quad (3.1)$$

$$U_w = U_s \quad \therefore Q_s = U_s \cdot A_s \quad (3.2)$$

$$\therefore V_c = \left(\frac{Q_s}{\text{Cross-sectional area of the strand}} \right) \quad (3.3)$$

where Q (m³/s) is the flow rate of both water (Q_w) and steel (Q_s), U (m/s) is the average flow velocity in the nozzle of both water (U_w) and steel (U_s), A (m²) is the cross-sectional area of nozzle in both water (A_w) and steel (A_s), and V_c (m/min) is the casting speed. Table 2.4 shows the casting speed in case of 230mm slab thickness x 1500mm slab width corresponding with water flow rate.

The mean active sites on the surface of porous refractory used in water model experiment are measured in Figure 2.21 with comparison to the measurements in stagnant flow as mentioned above. The mean liquid velocity of the downward flowing liquid in the nozzle is 1.25m/s. The point under downward flowing water in Figure 2.21 represents the range of mean active site from five replicate tests with same water model conditions. Figure 2.21 clearly shows the effect of downward flowing velocity on active sites. More active sites form under downward-flowing water than in stagnant water, due to the drag force from the water flow along the surface of porous refractory, which acts to shear the bubbles into the water stream before they grow up to the mature sizes found in stagnant flow. And the active site increases with increasing with gas injection flow rate. For same gas injection flow rate and water velocity in nozzle, the effect of permeability of porous refractory on active site is not clear, even though low permeability has slightly more active sites in stagnant flow.

The following empirical equation of the water model results can be used to estimate the mean active sites in downward-flowing water (S_{U_w}), the (dotted blue line in Figure 3.5):

$$S_{U_W} (\#/cm^2) = 2.31 \times \ln \left(\frac{Q_g}{A_{R_W}} \right) + 13.4 \quad (3.4)$$

where Q_g (SLPM) is the gas injection flow rate and A_{R_W} (cm²) is the surface area of refractory sample used in the water model.

C. Inner wall surface of real upper tundish nozzle

For the real upper tundish nozzle with the operating range of gas injection flow rate in the plant (Q_{g-Ar} , 5~11SLPM), the active sites on the inner wall surface area of real upper tundish nozzle can be obtained from the multiplication of estimated active sites and surface area ratio of real upper tundish nozzle to the porous refractory used in water model. Thomas *et al.*[60] have modeled that the distribution of argon gas velocity in the upper tundish nozzle after gas injection through one slit which is located near bottom, as shown in Figure 2.22. Therefore, the effective length (L_{eff}) which is exiting the bubbles on the inner wall was less than the actual length of upper tundish nozzle (L_{UTN}). In this study, the effective length was calculated as a 0.15m from the bottom of upper tundish nozzle compared to 0.24m actual length. Assuming that the shape of upper tundish nozzle is cylinder-like and bore diameter is 0.075m, the inner-wall surface area, (A_{R_Ar}), is 353.4cm².

In the actual caster, the gas expands to 99% of the molten steel temperature before it enters the liquid steel[61]. Thus, the gas flow rate leaving through each active site on the UTN refractory in the steel caster, Q_{g_site} , is easily converted from the nominal operating gas flow rate and the results of Equation (3.4) using Equation (3.5), as follows:

$$Q_{g_site} (ml / s / site) = \left(\frac{\beta \times Q_g}{A_{R_Ar} \times S_{U_W}} \right) \left(\frac{1000}{60} \right), \quad \text{where } \beta = \left(\frac{P_{Std} + \rho_S \cdot g \cdot H_S}{P_{Std}} \right) \left(\frac{T_{Std}}{T_S} \right) \quad (3.5)$$

In the Equation (3.5), β is the gas volume expansion factor, P_{Std} is the standard pressure, ρ_S is the density of steel, g is the gravitational acceleration,

H_S is the height of steel in the tundish above the UTN, T_{Std} is the standard temperature and T_S is the temperature of steel.

To match the gas injection flow velocity (SLPM/cm²) in both systems, 0.1, 0.2 and 0.3 SLPM used in water model experiments corresponds with 5.7, 11.5 and 17.2 SLPM in the plant respectively. Figure 2.23 relates the mean standard gas flow rate per unit surface area of UTN wall with the actual flow rate of hot argon gas per active site in the steel caster for the same three flow rates and three simulation gas flow rates. This work also gives new insight into similarity analysis of water and steel systems to aid in the design of future water models.

D. Bubble behavior in downward-flowing water

The water model measurements show that both the mean bubble size and the variation of its distribution increase with increasing gas injection flow rate, and decreasing water velocity, as shown in Figure 2.24. Decreasing water velocity below a critical minimum level (such as found in recirculation regions beneath the slide gate) allows the formation of very large bubbles [56]. The periodic release of such large gas pockets may cause large level fluctuations in the mold, leading to the entrapment of molten flux and other defects associated with an unstable meniscus.

E. Bubble size prediction in liquid steel

The size distribution of the argon bubbles was input according to a Rosin-Rammler diameter distribution in FLUENT[62]. For this method, the mean bubble diameter measured in the water model experiments were firstly modified to predict bubble diameters in the argon-steel system using the following equation from H. Bai [56],:

$$5.2692 \frac{\pi U}{Q_{g_hole} D_N^{1/17}} \int_{r_e}^{r_d} \left(r^{15/7} (ar+b)^{3/2} + \frac{ar^{22/7}}{2} (ar+b)^{1/2} \right) dr = 2r_d e_d^{3/2} + \frac{d}{2} - r_e \quad (3.6)$$

In this equation, U is the average liquid velocity in the nozzle (m/s), Q_{g_hole} is the gas injection flow rate per hole (ml/s/hole), D_N is the diameter of nozzle bore (mm), r is the horizontal radius of an ellipsoidal bubble (mm) at detachment (r_d) or the end of expansion (r_e), a and b are constants, e_d is the elongation factor at detachment as a function of U (m/s), and d is the gas injection hole diameter (mm). To enable use of this equation for porous refractory, the gas injection flow rate per active site was investigated with water model experiments.

Using Equation (3.6[56]) to predict the mean bubble diameter in the water model experiments, Figure 2.25 (black lines) show a reasonable agreement of trend with the present measurements (points) for different water velocities and gas flow rates. Figure 2.25 also shows the predicted mean bubble diameter in the liquid steel is larger than air bubble in water model, which is almost constant with these low gas flow rates. Figure 2.26 shows the mean bubble size predicted in the steel casting nozzle for different downward liquid velocities using Equation (3.6). With 2m/s mean argon liquid velocity in the nozzle, the mean bubble diameter predicted in Figure 2.26 is 2.3mm. Decreasing liquid velocity below a critical minimum level in the nozzle allows the formation of very large bubbles causing large meniscus fluctuation and slag entrapment. A Rosin-Rammler curve fit with 3 as the spread parameter using this diameter roughly matches the bubble size distribution measured in the water model, as shown in Figure 2.27(a). The corresponding mass fraction distribution, plotted in Figure 2.27(b) shows a bubble diameter range of ~5mm.

The mass flow rate of each bubble diameter was obtained from this mass fraction by multiplying it by the total gas mass flow rate, $\rho_{Ar} \cdot \beta \cdot Q_g$. Finally, the

number of bubbles injected per unit time with each diameter was obtained by dividing by the mass of each bubble. The entire distribution of the number of bubbles shown in Figure 2.27(a) contains 302 bubbles every 0.001sec at 9SLPM, which is injected from 302 random locations on the inner wall of the UTN each time step. From this way, 5 and 11SLPM contains 168 and 366 bubbles every time step respectively.

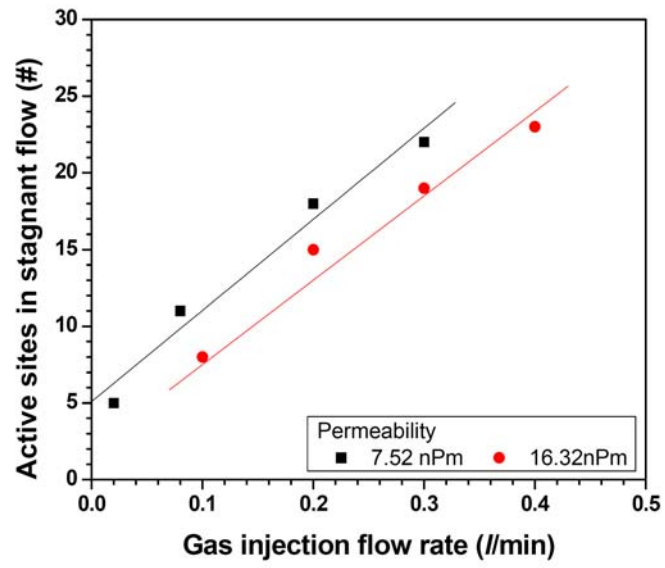


Figure 2.20 Active sites in stagnant water with different permeabilities of porous refractory

Table 2.4 Relationship of liquid flow rate between water model and steel
caster

Water flow rate (Q_w , SLPM)	28.2	32.5	36.8
Liquid velocity in nozzle ($U_w=U_s$, m/s)	0.96	1.10	1.25
Steel throughput (Q_s , m ³ /min)	0.25	0.29	0.33
Casting speed (m/min, 230mm thick x 1500mm wide)	0.74	0.85	0.96

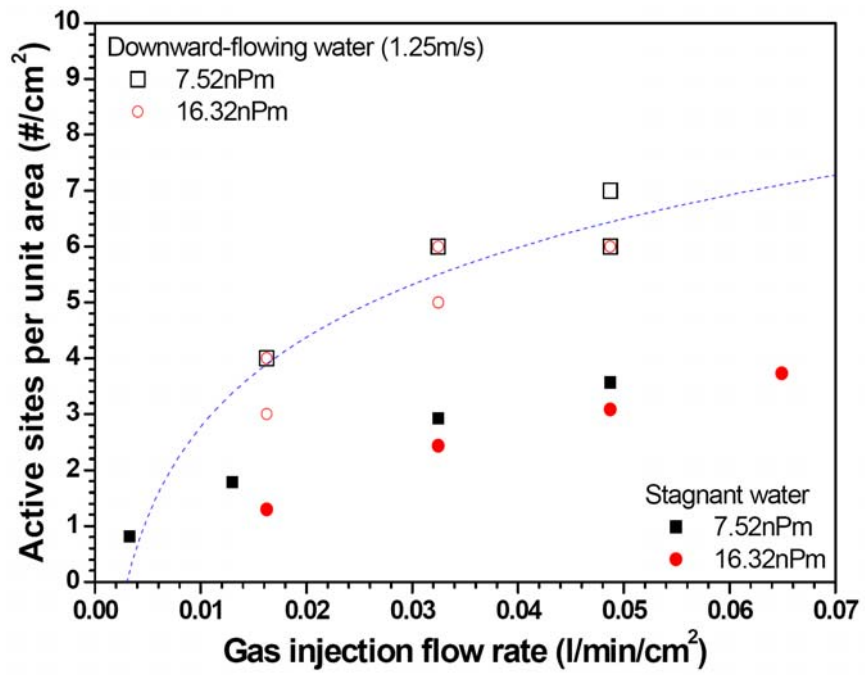


Figure 2.21 Active sites in both stagnant and downward-flowing water

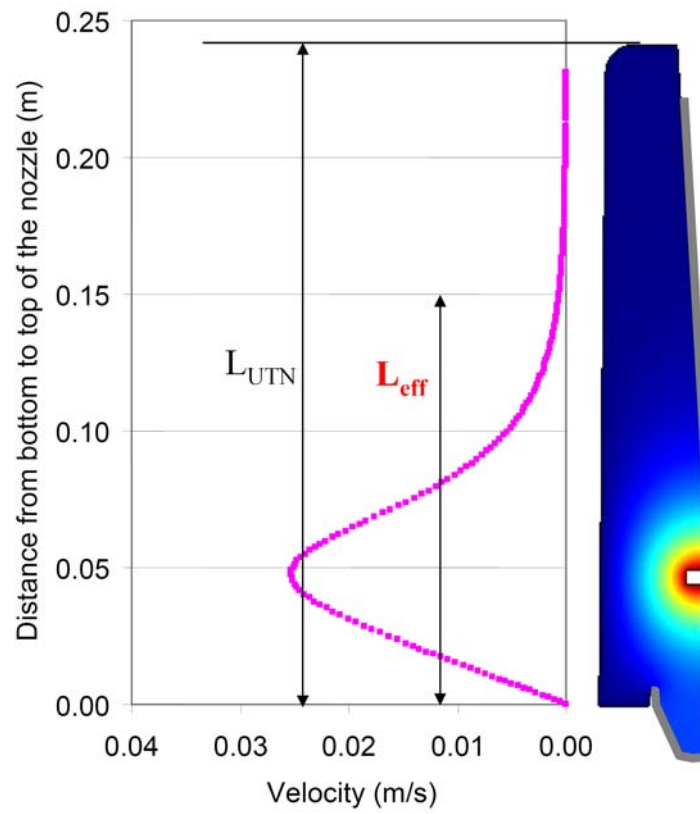


Figure 2.22 Distribution of argon gas flow velocity in the upper tundish nozzle[60]

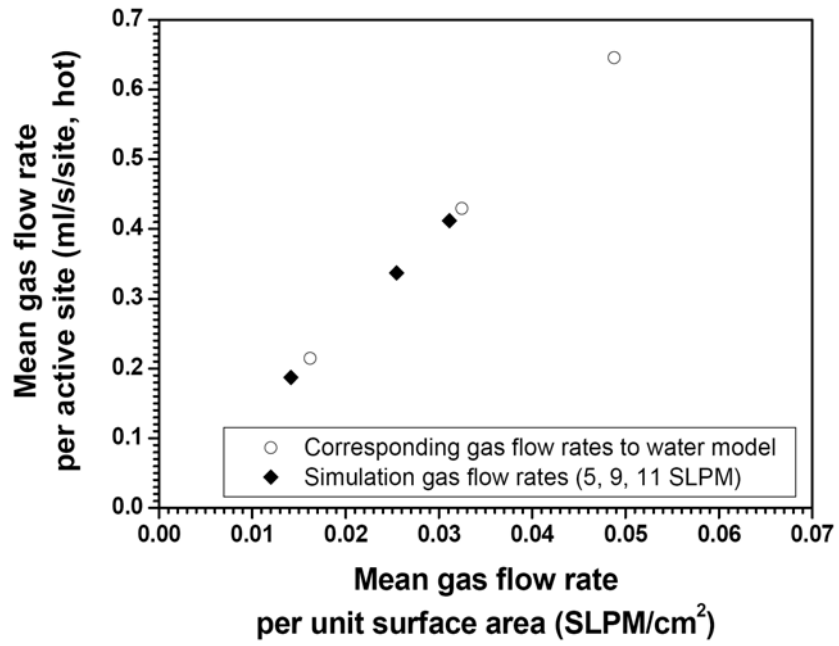


Figure 2.23 Relation of mean gas flow rate both per unit surface area of UTN wall and per active site in steel caster

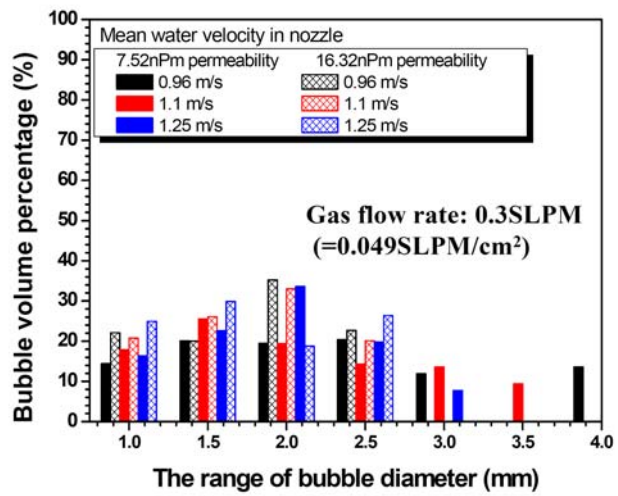
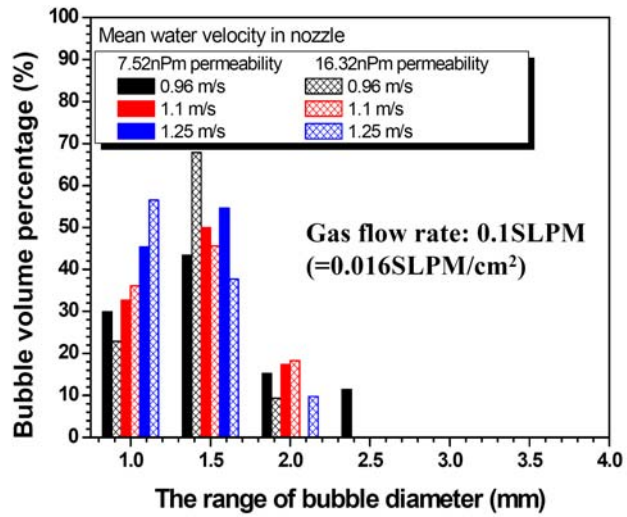


Figure 2.24 Bubble size distribution with different water velocity and gas flow rate (6.2cm² surface area of refractory sample)

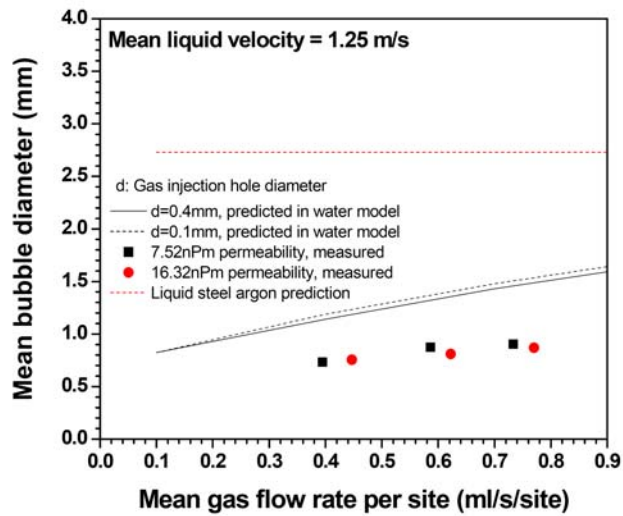
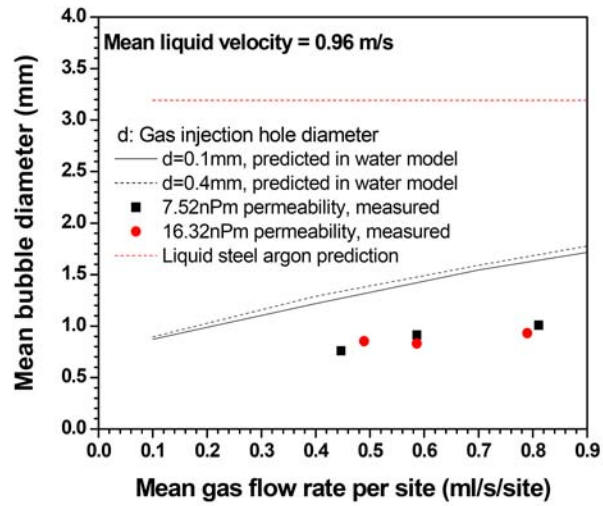


Figure 2.25 Comparison of bubble size between measurements and predictions in water model experiment

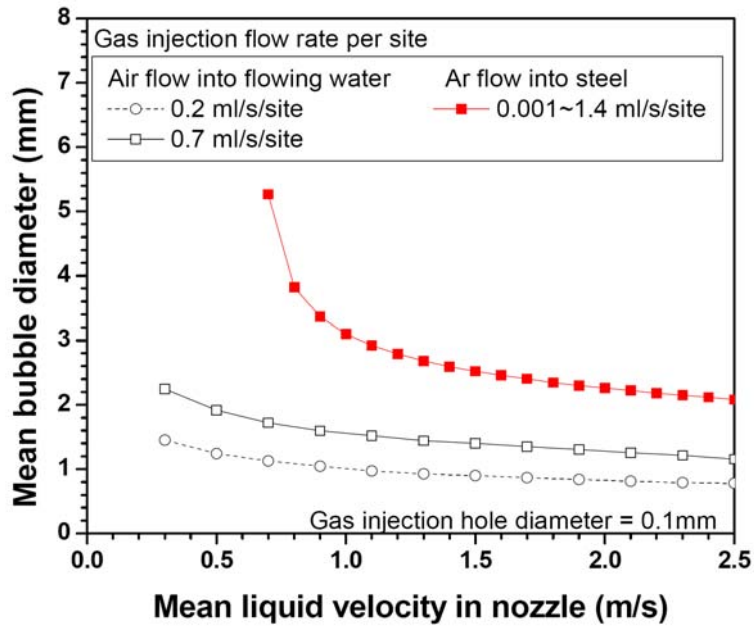


Figure 2.26 Prediction of bubble size in steel caster

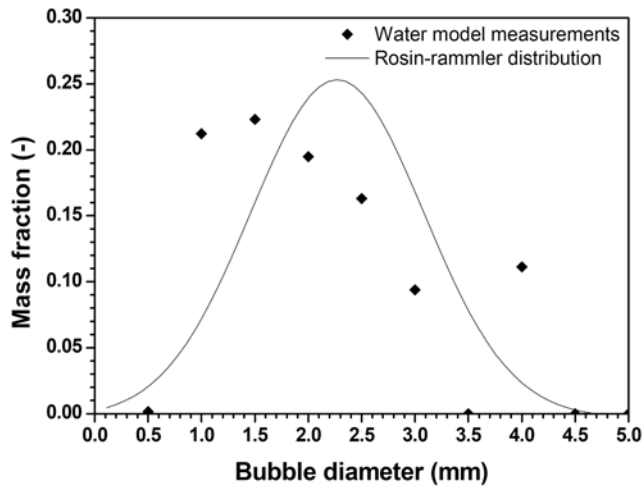
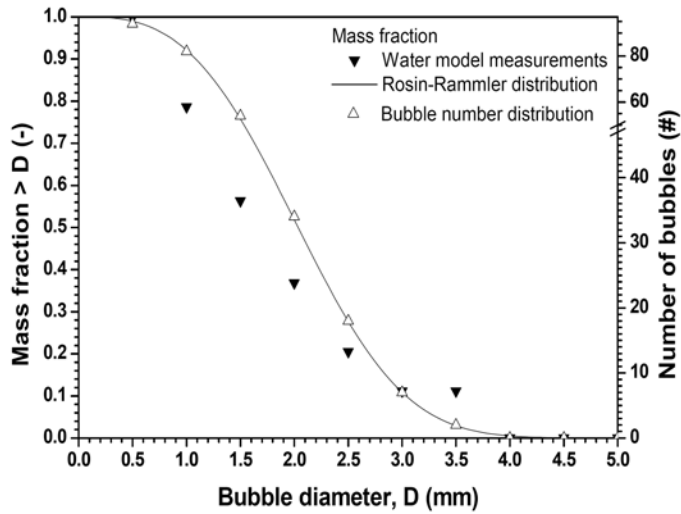
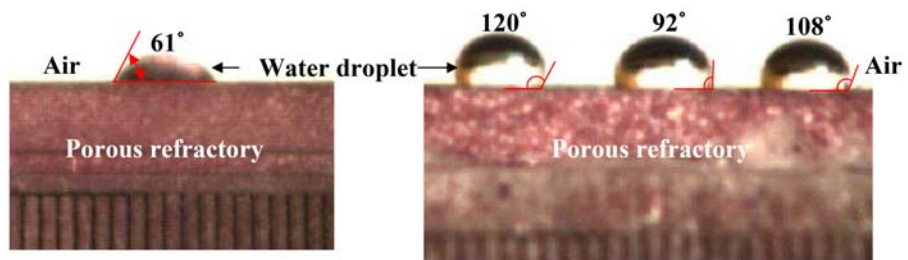


Figure 2.27 (a) Rosin-Rammler distribution of bubble diameters and number of bubbles and (b) corresponding mass fractions for 9SLPM

2.2.4 Surface coating of porous refractory

The wettability between the molten steel and the porous refractory through which argon gas was injected had a great influence on the behavior of the bubbles and the flow pattern of the molten steel inside the mold[63, 64]. To achieve the poor wettability (high contact angle) between water and porous refractory in water model experiment, the surface of porous refractory was coated by Silane solution (1,1,2,2-H-Perfluoro Dodecyltrichlorosilane) as a coupling agent. For this method, the active layer firstly was formed on the surface of porous refractory using O₂ plasma, and then was dipped in Silane solution. Figure 2.28 shows the change of contact angle after surface coating of porous refractory from 61 deg (uncoated) to ~107 deg (coated) and Figure 2.29 shows the evidence of coated elements on the surface of porous refractory using scanning electron microscope (SEM) for image analysis and electron dispersive x-ray spectroscopy (EDXS) for elemental analysis. Main couplers (Si, Cl) with surface oxygen were detected, showing the good coating process on the rough surface. Figure 2.30 shows how the number of active sites decreases sharply at higher gas flow rates after coating on refractory surface. The number of active sites with surface coating decreases, under same gas flow rate per site, which causes a lower frequency of bubble formation. This makes bubble formation has a much greater tendency to spread into a gas curtain over the refractory wall. The investigation of this phenomenon on the initial bubble formation and bubble behavior in the nozzle and mold needs much further work.



(a)

(b)

Figure 2.28 Contact angle (a) before surface coating, (b) after surface coating

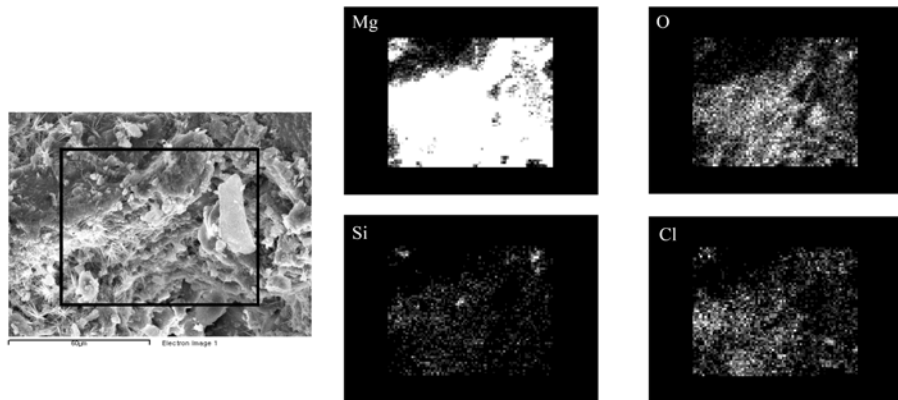


Figure 3.13 Elemental analysis showing the evidence of surface coating

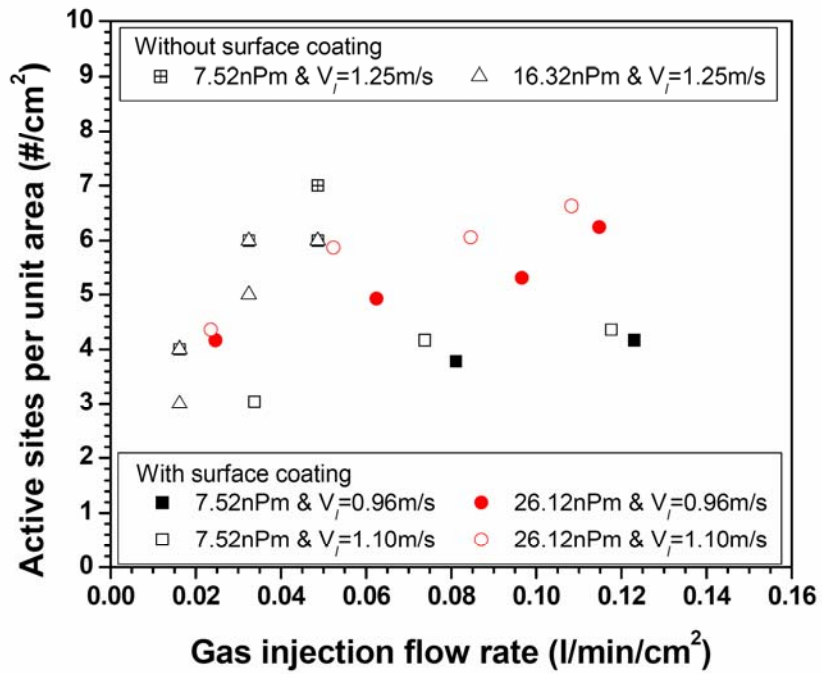


Figure 3.14 Comparison of active sites with and without surface coating of porous refractory in downward-flowing water

2.2.5 Summary

The initial stages of bubble formation from porous MgO refractory injecting gas into a downward turbulent liquid flow has been studied with water experiments. The active site which indicates the actual site exiting bubble on the surface of porous refractory was used for the effect of properties of refractory, and the similarity between water model experiments and steel caster. The bubble formation depends primarily on the velocity of the flowing liquid and secondarily on the gas flow rate.

Bubble size in a real nozzle is predicted using an analytical model and its distribution is developed using a Rosin-Rammler distribution function with parameters taken from measurements. The bubble size and distribution can be used for the multiphase simulation as discussed later.

Finally, the change of contact angle also affects the number of active sites in downward turbulent liquid flow, but much further works are needed for the investigation of initial bubble formation and bubble behavior in the nozzle and mold.

CHAPTER 3. Computational Modeling of Fluid Flow

A computational model has been developed to study the fluid flow phenomena in both the nozzle and mold. Owing to the left-right symmetry, the domain includes half of the nozzle and mold, extending from the tundish bottom to 3m below the meniscus, including both the inner and outer radius. To avoid the isotropic eddy-viscosity hypothesis of Boussinesq[65] and closes the Reynolds-averaged Navier-Stokes (RANS) models,[66] the Reynolds Stress Model (RSM)[67] to simulate turbulent fluid flow in three dimensions was used in solving the continuity equation and momentum transport equations for the Reynolds stresses and pressure, together with an equation for the dissipation rate, using the commercial computational fluid dynamics (CFD) package FLUENT. Discrete phase model (DPM) is used in Fluent to model the transport of particles in the nozzle and mold computational domain. Extensive user defined functions were written to modify the hydrodynamic forces acting on particles. The casting conditions and properties for the computational model are given in Table 3.1.

3.1 Governing equations for fluid flow

The steady-state, incompressible, three-dimensional time-dependent Navier-Stokes equations are solved in a Cartesian coordinate system for the velocity, pressure distributions in a nozzle and mold domain. The continuity equation for conservation of mass is

$$\nabla \cdot (\overline{\rho \vec{V}}) = 0 \quad (3.1)$$

where ρ is the density of steel and \vec{V} is the velocity.

The equation for conservation of momentum is

$$\nabla \cdot (\rho \vec{V} \vec{V}) = -\nabla p + \nabla \cdot \mu_{eff} (\nabla \vec{V}) + \rho \vec{g} \quad (3.2)$$

where p is the static pressure, $\vec{\rho g}$ is the gravitational force and μ_{eff} is the effective viscosity, calculated by

$$\mu_{eff} = \mu_o + \mu_t \quad (3.3)$$

where μ_o is the molecular viscosity, and μ_t is the turbulent viscosity.

The Reynolds-stress transport equations are written as follows;

$$U_k \frac{\partial}{\partial x_k} (\overline{u_j u_i}) = P_{ij} + d_{ij} + \phi_{ij} - \varepsilon_{ij} + \frac{\partial}{\partial x_k} \left(\nu \frac{\partial \overline{u_j u_i}}{\partial x_k} \right) \quad (3.4)$$

where P_{ij} is the production term, d_{ij} is the turbulent diffusion term of the Reynolds-stresses which is approximated by generalized gradient diffusion hypothesis[68], ϕ_{ij} is the pressure-strain redistribution term, and ε_{ij} is the dissipation rate of turbulence energy.

$$P_{ij} = - \left[\overline{u_j u_i} \frac{\partial U_j}{\partial x_k} + \overline{u_i u_j} \frac{\partial U_i}{\partial x_k} \right] \quad (3.5)$$

$$d_{ij} = \frac{\partial}{\partial x_k} \left[\frac{c_\mu k^2}{\sigma_k \varepsilon} \frac{\partial \overline{u_i u_j}}{\partial x_k} \right] \quad (3.6)$$

$$\varepsilon_{ij} = \frac{2}{3} \delta_{ij} \varepsilon \quad (3.7)$$

The turbulent scalar dissipation rate equation is computed with a model transport equation like as below;

$$\rho U_j \frac{\partial \varepsilon}{\partial x_j} = C_{\varepsilon 1} \frac{\varepsilon}{k} \left(-\rho \overline{u_i u_j} \frac{\partial U_i}{\partial x_j} \right) - C_{\varepsilon 2} \frac{\rho \varepsilon^2}{k} + \frac{\partial}{\partial x_j} \left(\left(\mu + \frac{\mu_t}{\sigma_\varepsilon} \right) \frac{\partial \varepsilon}{\partial x_j} \right) \quad (3.8)$$

The constant appearing in the above equation has the following values:

$$C_{\varepsilon 1} = 1.44, \quad C_{\varepsilon 2} = 1.92, \quad \sigma_k = 1.0, \quad \text{and} \quad \sigma_\varepsilon = 1.3$$

The pressure-strain term, ϕ_{ij} in the Equation (3.4) is modeled according to the proposal by Gibson and Launder[69] and approximates the process of

energy redistribution as a sum of three contributions:

$$\phi_{ij} = \phi_{ij,1} + \phi_{ij,2} + \phi_{ij,\omega} \quad (3.9)$$

where $\phi_{ij,1}$ is the slow pressure-strain term as the return-to-isotropy term, $\phi_{ij,2}$ is called the rapid pressure-strain term $\phi_{ij,\omega}$ is a correction accounting for the effects of wall induced pressure reflections.

The slow pressure-strain term, $\phi_{ij,1}$, is modeled as

$$\phi_{ij} = -C_1 \varepsilon b_{ij} \quad (3.10)$$

with $C_1 = 1.8$.

The rapid pressure term, $\phi_{ij,2}$, is modeled as

$$\phi_{ij,2} = C_2 \left[\left(\overline{u_i u_l} \frac{\partial U_j}{\partial x_l} + \overline{u_j u_l} \frac{\partial U_i}{\partial x_l} \right) - \frac{1}{3} \delta_{ij} \overline{u_i u_m} \frac{\partial U_l}{\partial x_m} \right] \quad (3.11)$$

with $C_1 = 0.6$.

The wall-reflection term, $\phi_{ij,\omega}$, is responsible for the redistribution of normal stresses near the wall and modeled as

$$\begin{aligned} \phi_{ij,\omega} = & C_1 \frac{\varepsilon}{k} \left(\overline{u_k u_m} n_k n_m \delta_{ij} - \frac{3}{2} \overline{u_i u_k} n_j n_k - \frac{3}{2} \overline{u_j u_k} n_i n_k \right) f \\ & + C_2 \left(\phi_{km,2} n_k n_m \delta_{ij} - \frac{3}{2} \phi_{ik,2} n_j n_k - \frac{3}{2} \phi_{jk,2} n_i n_k \right) f \end{aligned} \quad (3.12)$$

where $C_1 = 0.5$, $C_2 = 0.3$.

The turbulent viscosity, μ_t , is computed using the following equation:

$$\mu_t = \rho C_\mu \frac{k^2}{\varepsilon} \quad (3.13)$$

wall-reflection term, $\phi_{ij,\omega}$, is responsible for the redistribution of normal stresses near the wall and modeled.

The governing equations are discretized in FLUENT using a first-order

upwinding implicit scheme for unsteady formulation, segregated solver to solve the discretized equations, and SIMPLE algorithm for pressure-velocity coupling.[70]

3.2 Bubbles in fluid flow

Particle transport due to turbulence in the fluid phase can be predicted using the stochastic tracking (random walk) model including the effect of instantaneous turbulent velocity fluctuation on the particle trajectories in the discrete phase model in FLUENT.

Modeling of liquid-particle flow can be classified as “one-way” turbulence coupling, where the flow affects the particle motion, or “two-way” coupling, if the particles also modify the flow. Thus, while the continuous phase always impacts the discrete phase, the effect of the discrete phase trajectories should be incorporated on the continuum. Two-way coupling is important for gas flows with heavy particles. This two-way coupling is accomplished by alternately solving the discrete and continuous phase equations until the solutions in both phases have stopped changing.

Lagrangian motion of liquid-particle flows is used in this study to model particle motion categorized with “two-way” coupling.

The trajectories of bubbles in FLUENT can be predicted by integrating the force balance on the bubbles, which is written in a Lagrangian reference frame. This is given as follows:

$$m_b \frac{d\vec{v}_b}{dt} = \vec{F}_D + \vec{F}_L + \vec{F}_{Press} + \vec{F}_{Stress} + \vec{F}_A + \vec{F}_G \quad (3.14)$$

where m_b is the mass of bubble, v_b is the bubble velocity, \vec{F}_D is the drag force, \vec{F}_L is the shear lift force, \vec{F}_{Press} is the pressure gradient force, F_{Stress} is the stress gradient force, \vec{F}_A is the added mass term, \vec{F}_G is the

gravitational force. Assuming the spherical bubbles in the expression, the momentum of bubble is small. So $\overline{F_{Press}}$, $\overline{F_{Stress}}$, and $\overline{F_A}$ forces are quite small, and then negligible.

3.2.1 Drag force

The drag force acting on spherical bubble across the field of steady state fluid is as follows[71]:

$$\overline{F_D} = \frac{1}{8} \pi d_b^2 \rho_f C_D |\overline{v_f} - \overline{v_b}| (\overline{v_f} - \overline{v_b}) \quad (3.15)$$

where $C_D = \left(\frac{24}{Re_b} \right) f_{Re_b}$ and the Reynolds number of bubble is defined as

$$Re_b = |\overline{v_f} - \overline{v_b}| \frac{d_b}{\nu} \quad (3.16)$$

where, v_f is the velocity of fluid flow, v_b is the velocity of the bubble, C_D is known as the drag coefficient, Re_b is the Reynolds number of bubble and f_{Re_b} is the correction factor due to a finite Reynolds number of bubble and can be found as follows under $Re_p \leq 200$ [71]:

$$f_{Re_p} = (1 + 0.15 Re_p^{0.687}) \quad (3.17)$$

3.2.2 Shear lift force

Saffman[72] derived the lift force on solid spheres in an unbounded linear shear flow with the following expression:

$$F = 6.46 \rho_f \nu_f^{1/2} v_{r\infty}^2 r_b^2 \omega^{1/2} \quad (3.18)$$

where ρ_f is the fluid density, ν_f is the fluid kinematic viscosity, r_b is the radius of bubble, $v_{r\infty}$ is the relative velocity of bubble and fluid measured on the streamline through the center, and ω is the magnitude of velocity

gradient. In this equation, it is assumed that lift force on a sphere moving through a very viscous liquid with velocity $v_{r\infty}$ relative to a uniform simple shear.

This restriction was relaxed by Mclaughlin[73] and modified the expression for shear lift force.

$$F = 6.46\rho_f v_f^{1/2} v_{r\infty} R_b^2 \left(\frac{J}{2.255} \right) \omega^{1/2} \quad (3.19)$$

The general expression for J is as follows:

$$J = 2.255 - 0.6463 / \varepsilon_\infty^2 \text{ for } \varepsilon_\infty \gg 1 \text{ or } J = 32\pi^2 \varepsilon_\infty^5 \ln(\varepsilon_\infty^2) \text{ for } \varepsilon_\infty \ll 1 \quad (3.20)$$

The parameter, ε_∞ , is defined as

$$\varepsilon_\infty \equiv \frac{N_{R_c \omega \infty}^{1/2}}{N_{R_c \infty}} \quad (3.21)$$

where $N_{R_c \infty} \equiv \frac{|v_{r\infty}| d_b}{\nu_f}$, $N_{R_c \omega \infty} \equiv \frac{|\omega| d_b^2}{\nu_f}$ (d_b is the diameter of bubble).

The expression for J is rather complicated by Mclaughlin[73], therefore Mei[74] reconstructed it using curve fitting for $0.1 \leq \varepsilon \leq 20$:

$$J(\varepsilon_\infty) = 0.6765 \{1 + \tanh[2.5 \log_{10} \varepsilon_\infty + 0.191]\} \times \{0.667 + \tanh[6(\varepsilon_\infty - 0.32)]\} \quad (3.22)$$

3.2.3 Gravitational force

The gravitational force due to the buoyancy force of the density difference between fluid and bubble can be written as follows:

$$F_G = \frac{1}{6} \pi d_b^3 \rho_b g \quad (4.23)$$

3.3 Boundary conditions

3.3.1 Nozzle inlet

Across the inlet plane at the top of the nozzle, the inlet velocity value is set, based on the mass flow required to achieve the desired casting speed:

$$V_{avg} = \frac{A_{mold}}{A_{inlet}} * V_{cast} \quad (4.24)$$

Boundary values for the turbulent kinetic energy, k , and its dissipation rate, ϵ , also must be specified. The best inlet condition is to extend the domain upstream to model a portion of the bottom of the tundish, so that appropriate values evolve at the top of the nozzle. To simulate geometries with no tundish region, previous values have been calculated from a mixing length model for turbulent pipe flow.[75] As the flow near the bottom of the tundish region is fairly slow relative to the nozzle inlet, its turbulent intensity is less, so small inlet values of $\sim 10^{-5}$ are appropriate to be used for the turbulent kinetic energy and its dissipation rate respectively.

3.3.2 Nozzle and mold outlet

H. Bai *et al.* showed that using pressure boundary conditions allows for an accurate flow simulation, including the velocities near the outlet boundaries.[76] These outlet conditions allow recirculation zones to appear at the outlets, which has a large effect on flow in the domain. Gage pressure at both the nozzle and the mold outlets was set to zero, which is an arbitrary value that acts as a reference pressure for the rest of the domain.

3.3.3 Mold inlet

The text file containing of the values of velocity components, turbulence kinetic energy, turbulence dissipation rate and Reynolds stresses at each node from the nozzle outlet was written. This file was then read into commercial CFD program FLUENT, version 6.2.16, and the values were used as the mold

inlet conditions for the mold simulations.

3.3.4 Wall

In order to avoid excessive mesh refinement near the wall, a no slip boundary condition and standard wall boundary functions are applied on the inner walls of the nozzle in the nozzle simulation and the exterior walls of the nozzle, and mold walls in the mold simulations.[62] As the flow remains fully turbulent throughout the nozzle and mold, this condition is reasonable. Solidification of the shell in the mold was neglected, owing to its minor effect to the fluid flow of the thick mold of interest in this work.

A no slip boundary condition with wall laws for turbulence[62] is applied to all walls except at the mold top surface. A free slip condition (zero shear stress) is imposed on the mold top surface. This neglects the slight effect of slag layer, which tends to slow flow across the top.

3.3.5 Solution procedure

The governing equations are discretized in FLEUNT using an implicit, first-order upwinding scheme and the SIMPLE algorithm for pressure-velocity coupling[62]. FLUENT's segregated solver is used to solve the discretized equations in the following order. Initial conditions (if calculating the first iteration) or values from the previous iteration step are used to solve for the velocities in each cell using the conservation of momentum equations. The continuity equation is then imposed to correct any mass-flow imbalances present in the cells. Convergence is taken to be achieved when the total scaled residual drops below 10^{-5} , due to the minor change of the flow pattern below this value. The User Defined Function (UDF) is compiled to impose the forces acting on the bubbles in FLUENT.

3.4 Fluid flow in nozzle

The purpose of the slide gate is to control the flow rate. The model domain of typical nozzle geometry with slide gate control system (used at POSCO) includes some tundish region along with the nozzle as can be seen in Figure 3.1. Two different views of the nozzle mesh structured hexahedral cells can be seen in Figure 3.2. The inlet velocity direction is chosen this time so as to ensure there is no asymmetry because of the flow in the tundish so as to isolate the asymmetries caused by the slide gate. Steel enters the tundish region in radial direction. The inlet velocity has been set as to a value of 0.014 m/s which gives a flow rate of 61.68kg/s to provide a casting speed of 1.46m/min for a mold of dimensions 230mm thick x 1570mm wide. The inlet turbulence kinetic energy and dissipation rate values are set to $1e^{-4}m^2/s^2$ and $1e^{-4}m^2/s^3$ respectively. The inlet of UU, VV, WW Reynolds stresses are set to $1e^{-5}m^2/s^2$, and UV, VW, UW Reynolds stresses are set to 0. The solution converges in about 700 iterations.

Bubble size and its distribution for multiphase fluid flow in the nozzle were taken by Rosin-Rammler function based on water model measurements with three different gas flow rate at UTN (5, 9, and 11SLPM), as discussed in Chapter 2 and each bubble is located at random position on the UTN inner wall.

Figure 3.3 shows velocity magnitude contours computed in the nozzle (both front and side views) for different gas flow rates into the UTN. The recirculation region beneath the slide gate increases with increasing argon injection flow rate. The concentration of gas in the recirculation region also increases, as shown in Figure 3.4, likely leading to large gas pockets. This phenomenon leads to asymmetric flow at the nozzle outlet right port, as shown in Figure 3.5 and 3.6. More gas exits the right top of the right nozzle port, while stronger steel flow exits the right bottom side of the right nozzle. Higher

gas injection flow rate produces stronger asymmetric recirculation flow at the nozzle outlet ports.

Bubble concentration is higher at the upper regions of the nozzle outlet ports, owing to accumulation of the buoyant phase in the low-velocity regions there, as shown in Figure 3.4. The coalescence of bubbles in this region may cause large bubbles to form there, as clearly observed in the water model experiment in Figure 3.7. Later, the periodic rupture of these large escaping gas pockets at the slag-steel interface at the top surface of the mold can cause unstable meniscus behavior, level fluctuations, and corresponding surface defects.

Table 3.1 Simulation conditions and materials properties used in this calculation

Mold size	230mm thick x 1570mm wide x 3000mm long
Casting speed	1.46m/min (Average liquid velocity in nozzle: 2m/s)
Submerged Entry Nozzle type	Bifurcated
SEN submergence depth	180mm
Nozzle port height x thickness	98mm x 70mm
Nozzle bore diameter	75mm
Nozzle port angle	35 degree downward
Density of molten steel	7020kg/m ³
Viscosity of molten steel	0.0067kg/m·s
Argon gas flow rate	5, 9 and 11 SLPM
Density of argon gas at 1560°C	0.446kg/m ³

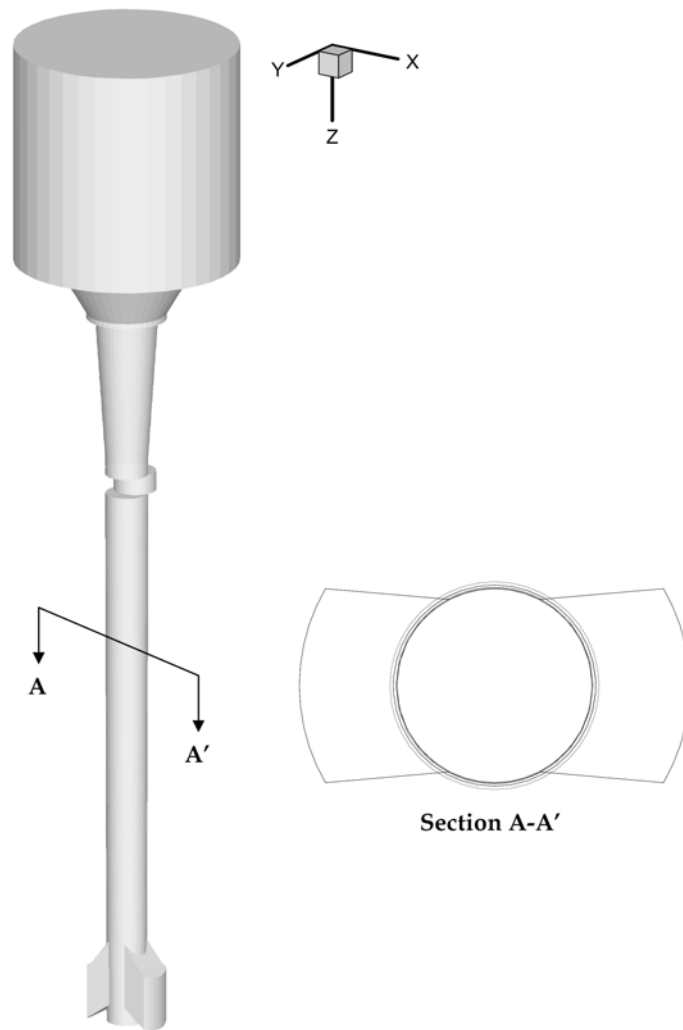


Figure 3.1 Schematic of the nozzle geometry with slide gate used in Gwangwang Works, POSCO

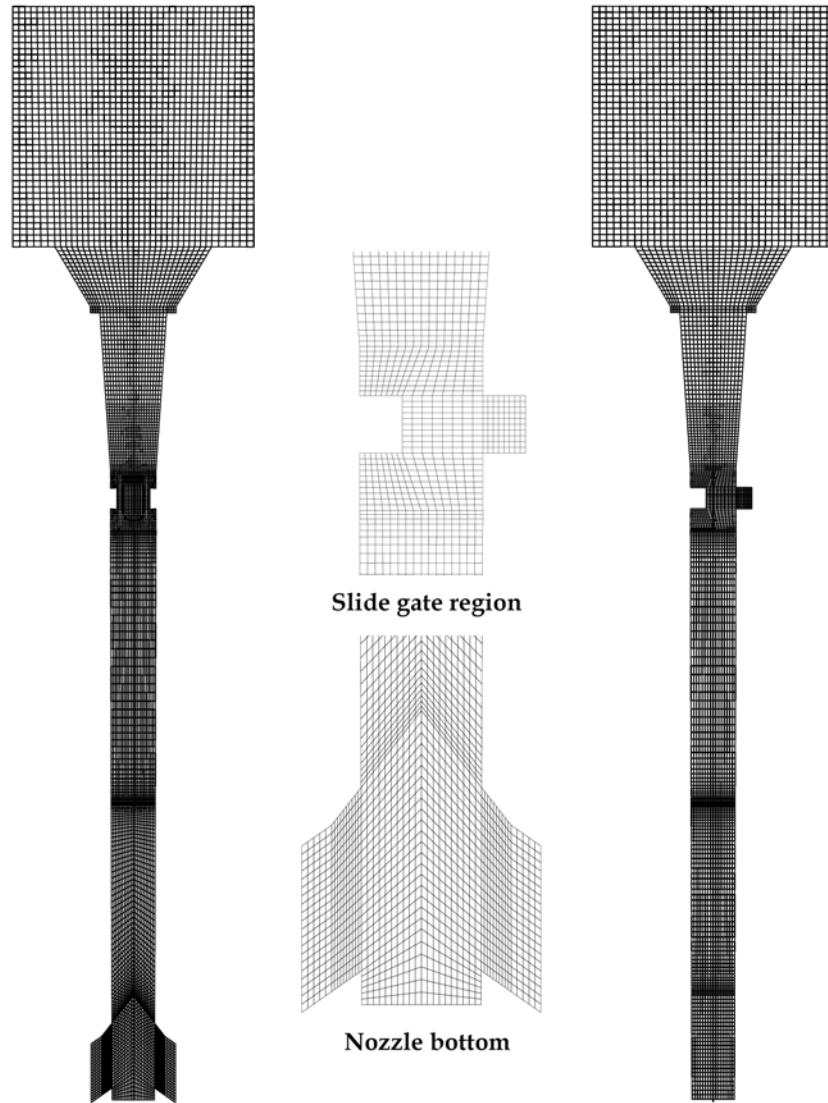


Figure 3.2 Nozzle mesh at different sections with slide gate

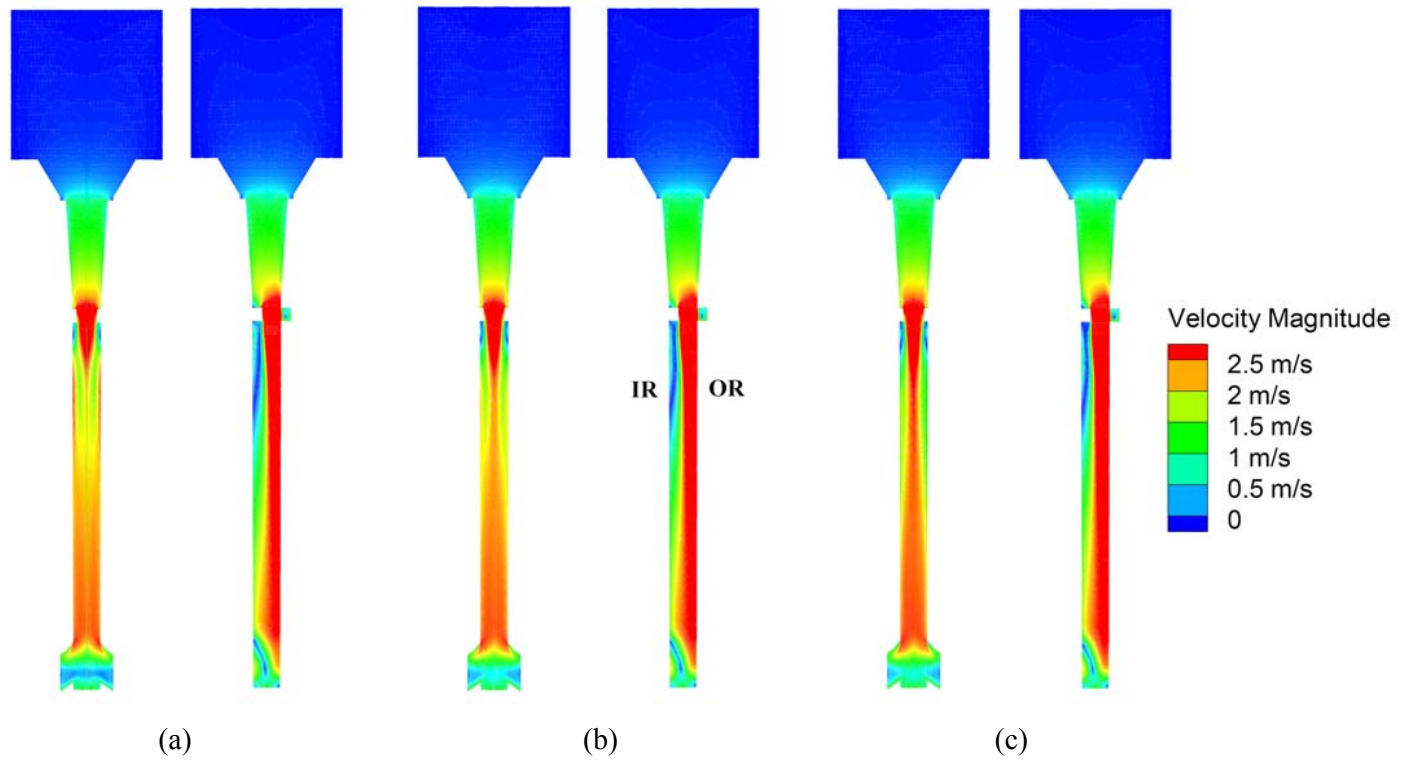


Figure 3.3 Velocity magnitude distribution in the nozzle with different gas flow: (a) 5SLPM, (b) 9SLPM and (c) 11SLPM (IR: Inner radius, OR: Outer radius)

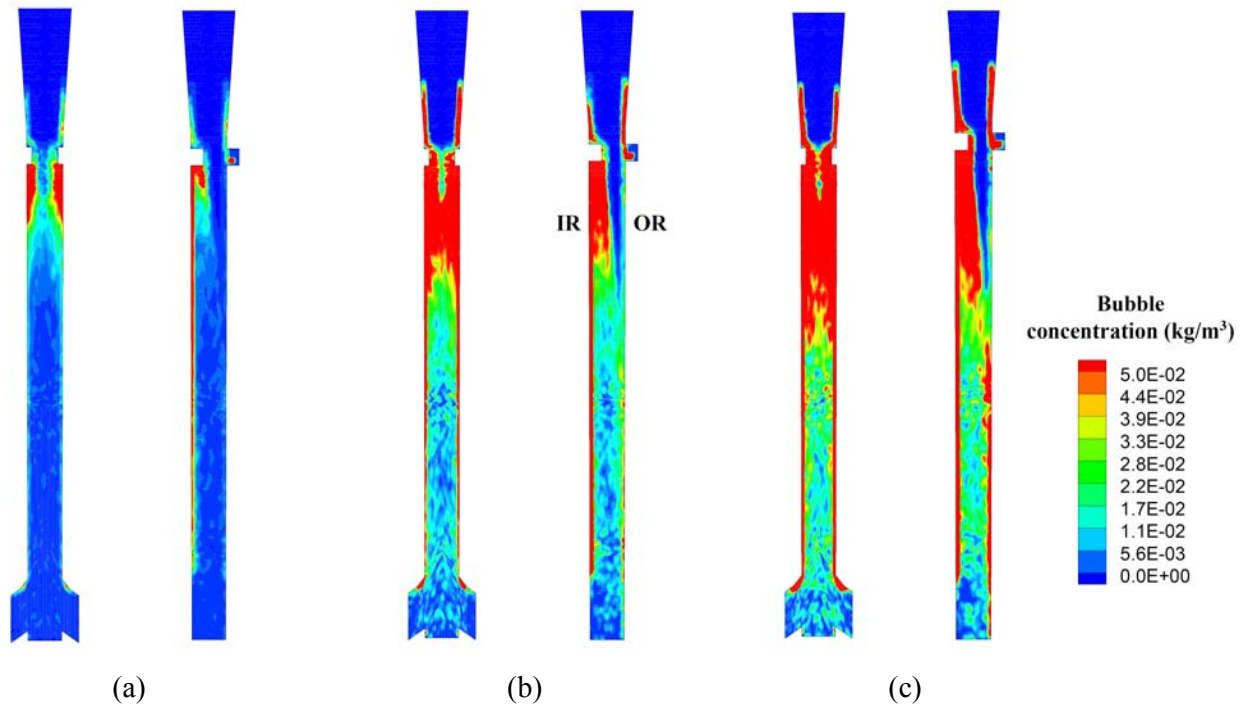


Figure 3.4 Bubble concentration in the nozzle:
 (a) 5SLPM, (b) 9SLPM and (c) 11SLPM

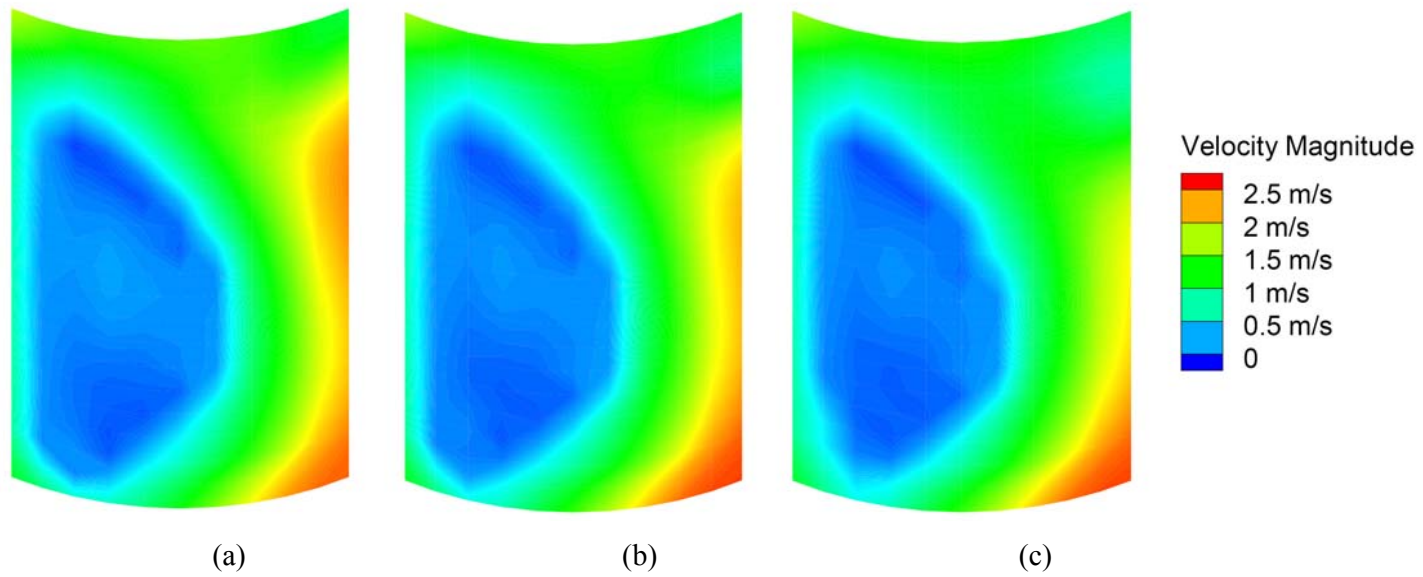


Figure 3.5 Velocity magnitude contour at right nozzle port:

(a) 5SLPM, (b) 9SLPM and (c) 11SLPM

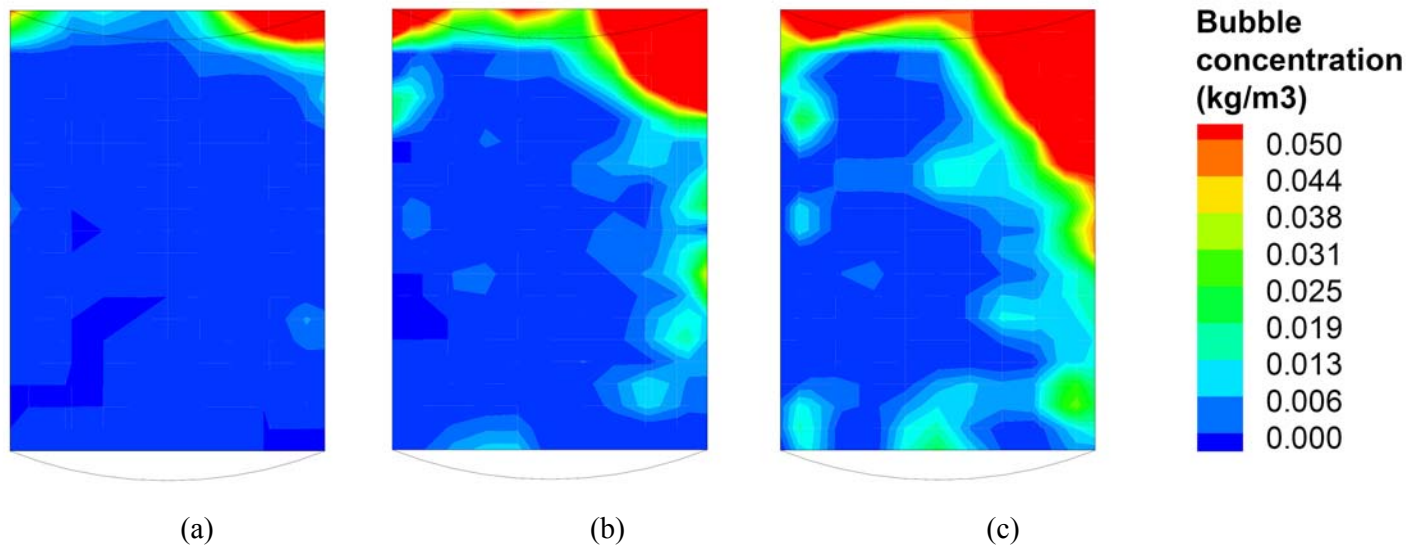


Figure 3.6 Bubble concentration contour at right nozzle port:
(a) 5SLPM, (b) 9SLPM and (c) 11SLPM

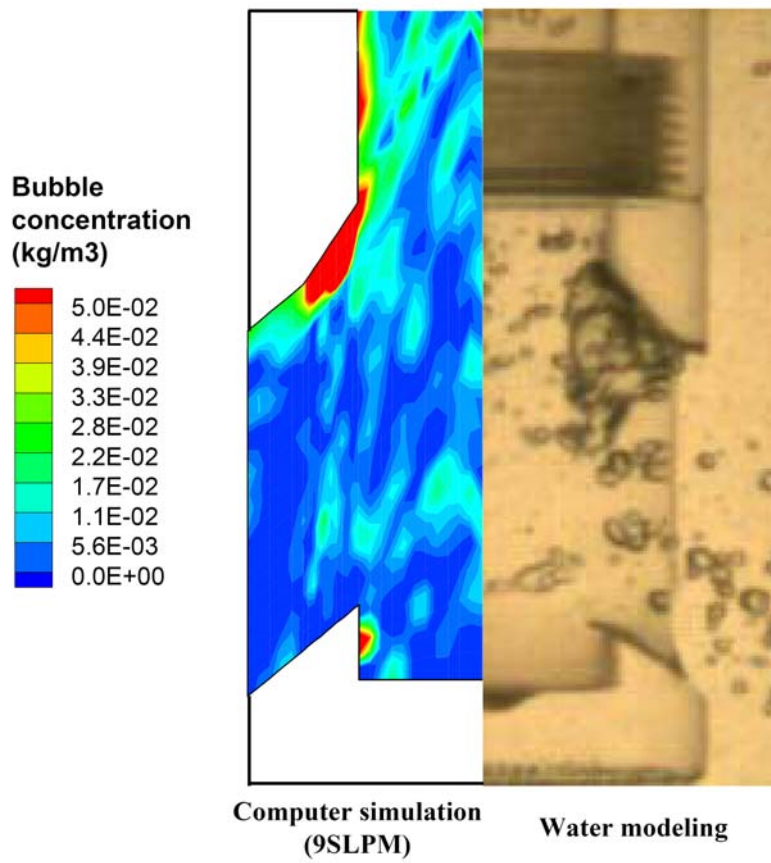


Figure 4.7 Big bubble formation in recirculation flow

3.5 Fluid flow in mold

To investigate the reason of the asymmetric flow from nail board dip tests and the asymmetric distribution of entrapped particles from ultra-sonic analyzer with different gas flow rate, the half mold simulation was conducted after gas injection as shown in Figure 3.8. Figure 3.9 ~ 12 show the velocity profiles with three different planes at 50sec after starting gas injection at the UTN with different gas flow rate. The flow after impingement to narrow face is moving up along outside wide face, and then the flow is moving down along the inside wide face after cross the top surface at higher gas flow rate.

Figure 3.13 shows bubble concentrations in the mold at 50sec after starting gas injection at the UTN with different gas flow rate. The concentration near the SEN is higher due to the rapid diffusion of gas bubbles, and their flotation up the outside radius face to be removed at the top surface. The distribution of gas bubbles on the top surface is greatly affected by the asymmetric flow at the nozzle outlet port, as mentioned above. Asymmetric flow from the nozzle port directs flow up the outside radius face. At the same time, the buoyancy of the gas-rich fluid concentrated near the outer-radius side of the SEN greatly exacerbates the flow asymmetry, by lifting the fluid up the outside radius. Figure 3.14 ~ 16 shows the three dimensional view of bubble concentration at that time in a half mold. These results match well with the surface velocity profile and the distribution of entrapped particles from plant measurements, as mentioned earlier.

This is because capture criterion of bubbles established by Quan *et al.* [77]. The particles smaller than the primary dendrite arm spacing (PDAS) can be easily captured into the solidification front, when the particle approaches. Otherwise, the capture criterion showed that particles larger than the PDAS can only be captured into the solidification front when the fluid is stagnant at front of dendrite from force balance between buoyancy force and drag force as

shown in Figure 3.17. With a range of bubble sizes, there is always one size with a rising velocity that exactly matches the downward flow velocity, so is suspended in front of the solidification front near the inner radius, and becomes captured.

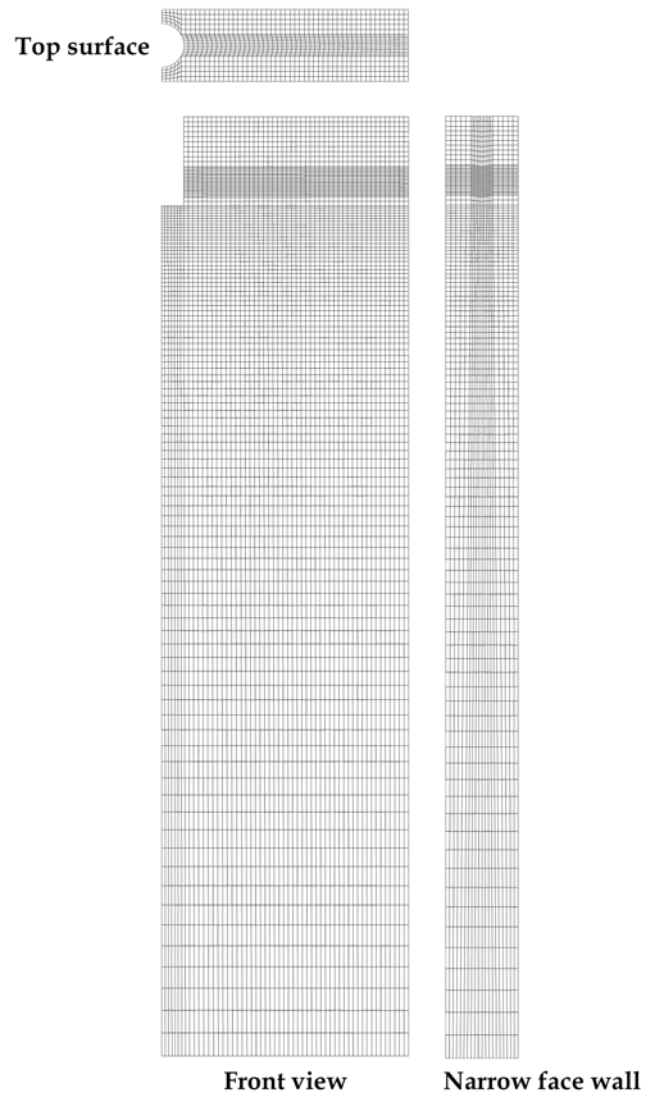


Figure 3.8 Half mold mesh without shell

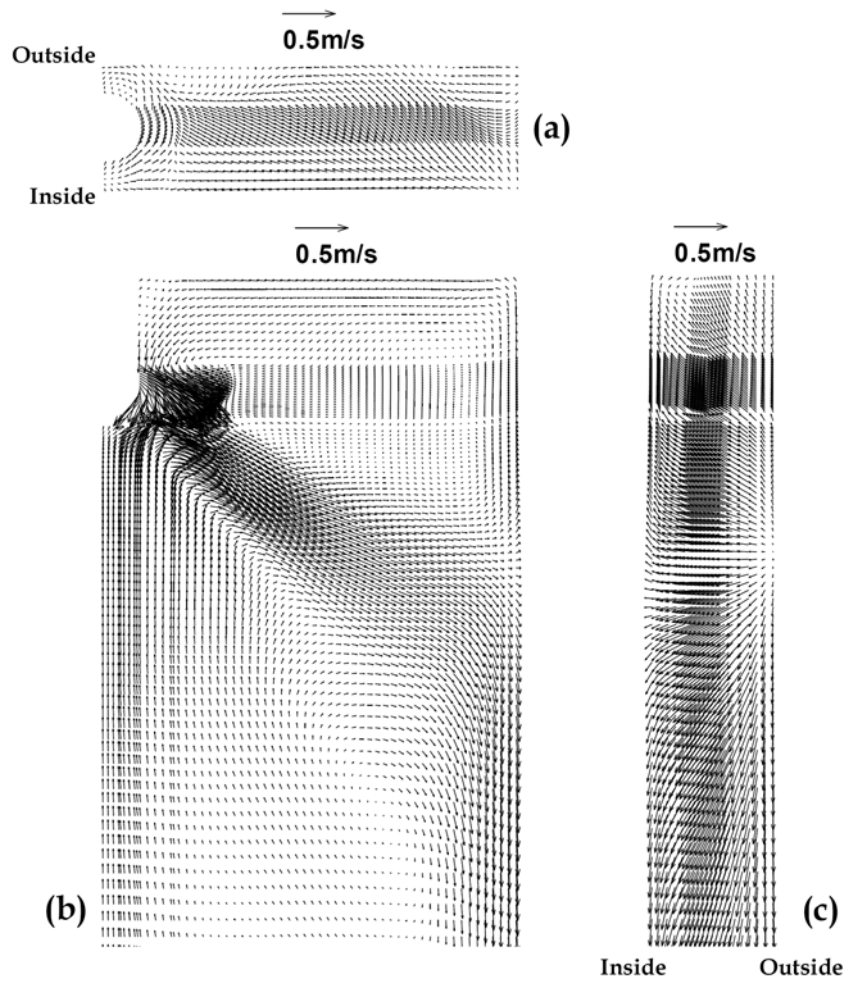


Figure 3.9 Velocity vector profile at 50sec after argon gas injection with 5SLPM:(a) top surface,(b) center plane between wide faces and (c) narrow face

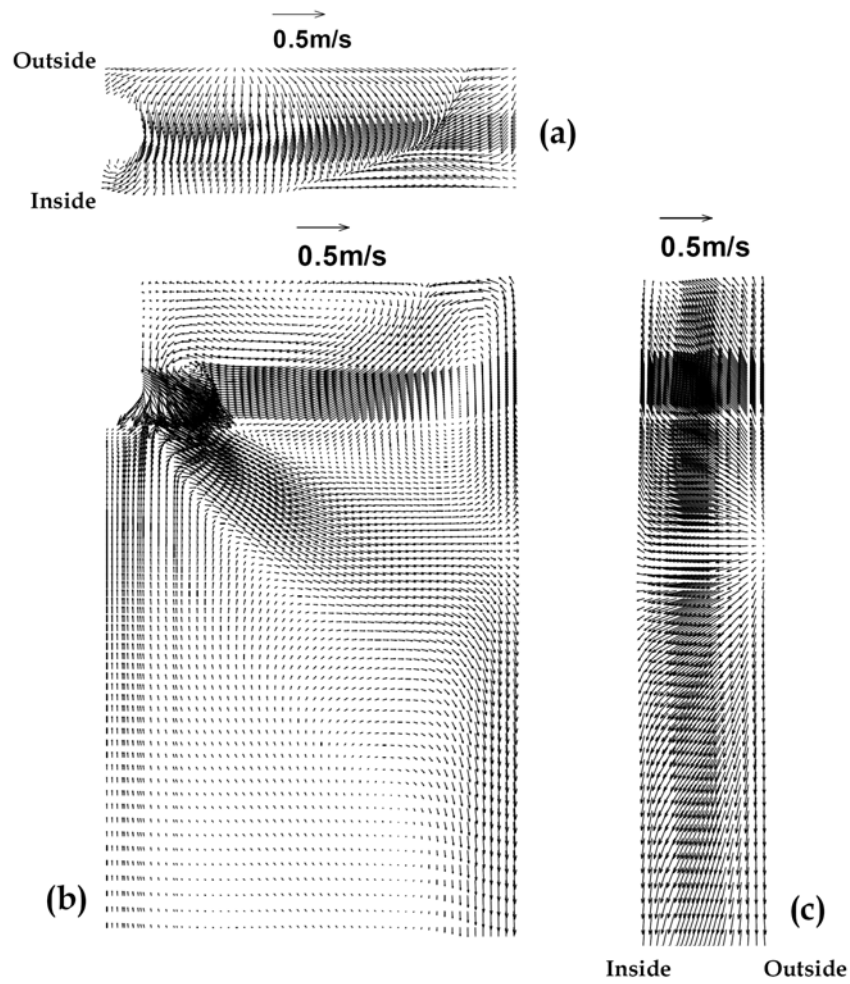


Figure 3.10 Velocity vector profile at 50sec after argon gas injection with 9SLPM:(a) top surface,(b) center plane between wide faces and (c) narrow face

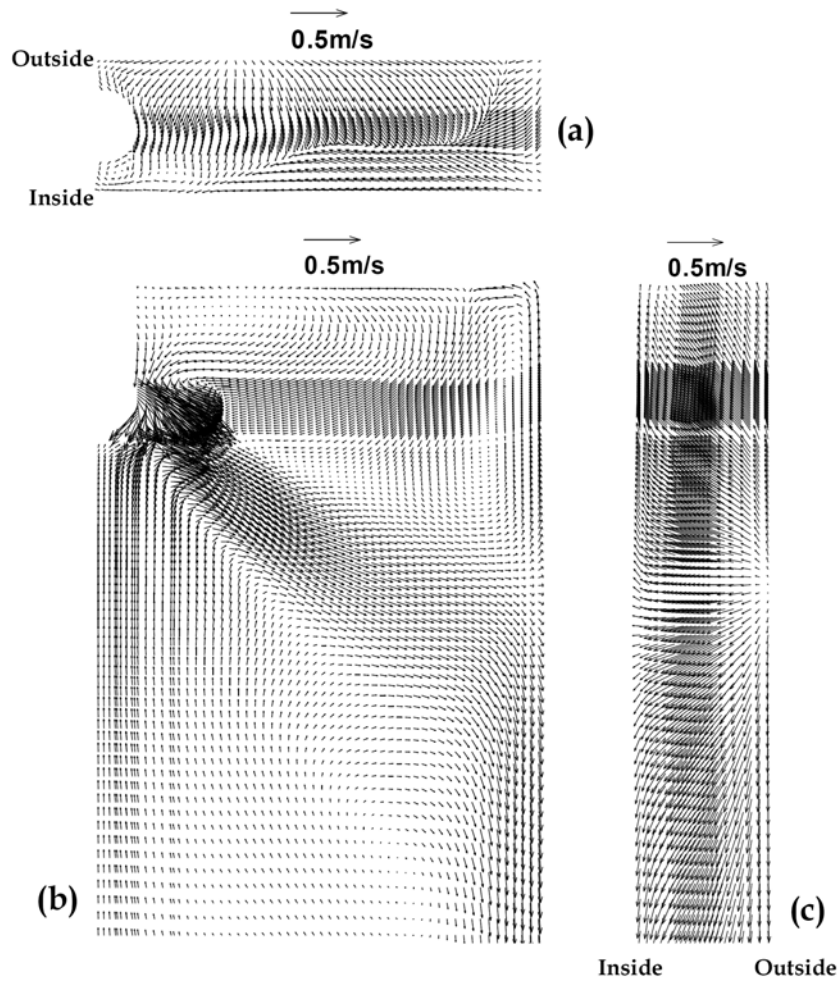


Figure 3.11 Velocity vector profile at 50sec after argon gas injection with 11SLPM:(a) top surface,(b) center plane between wide faces and (c) narrow face

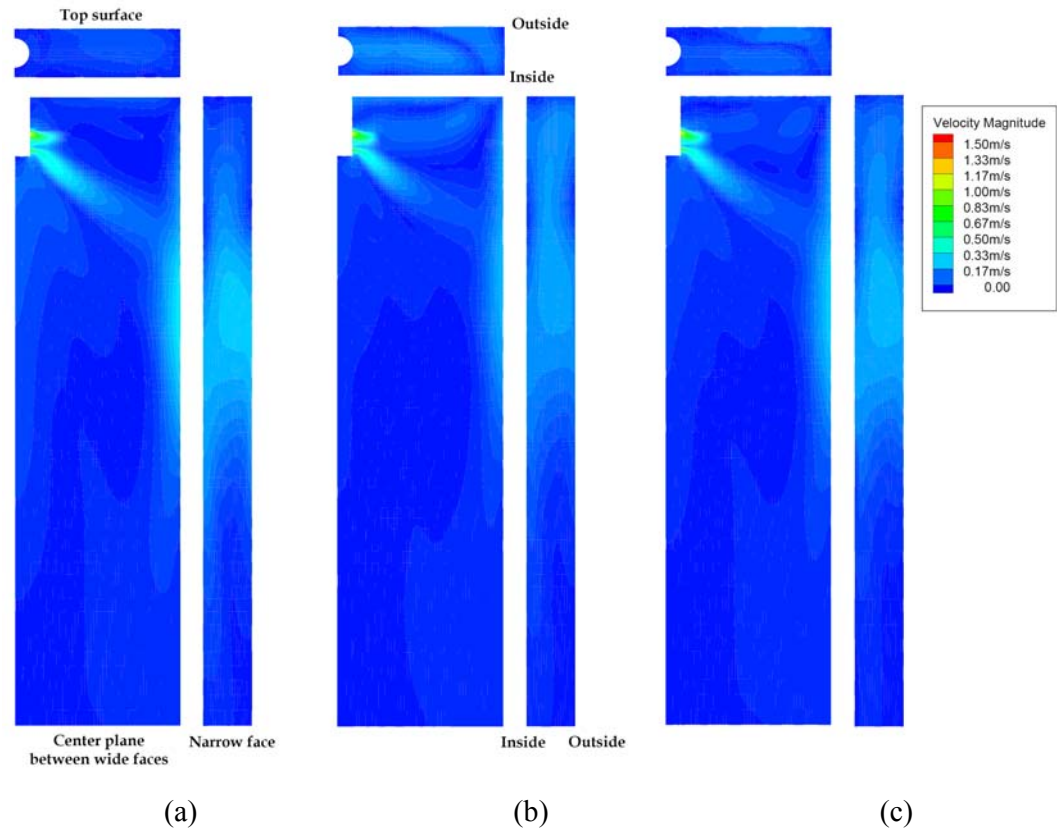
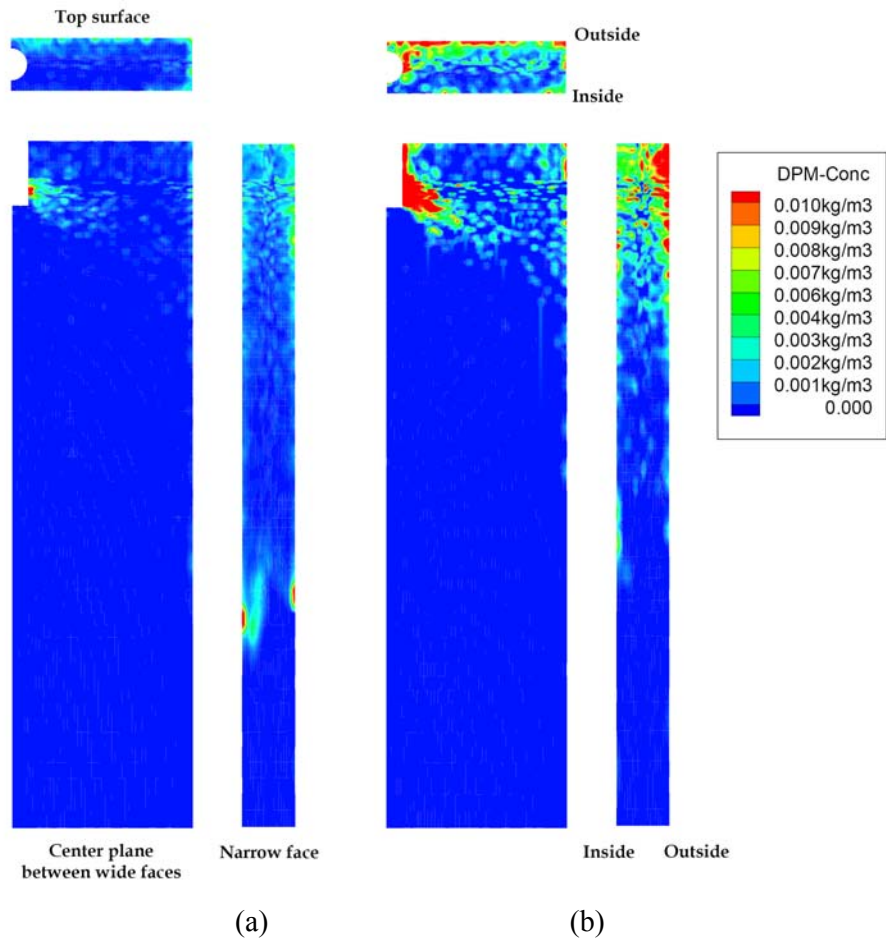
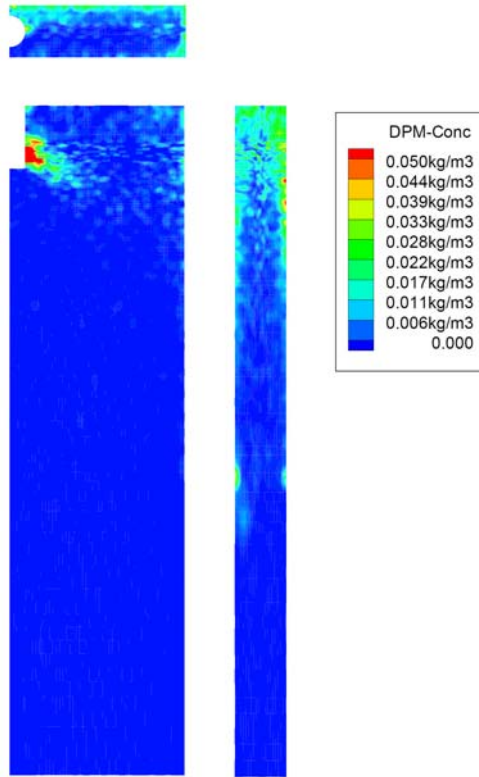


Figure 3.12 Velocity magnitude profiles with different view at 50sec after argon gas injection: (a) 5SLPM, (b) 9SLPM and (c) 11SLPM





(c)

Figure 3.13 Bubble concentration in half mold at 50sec after gas injection:

(a) 5SLPM, (b) 9SLPM and (c) 11SLPM

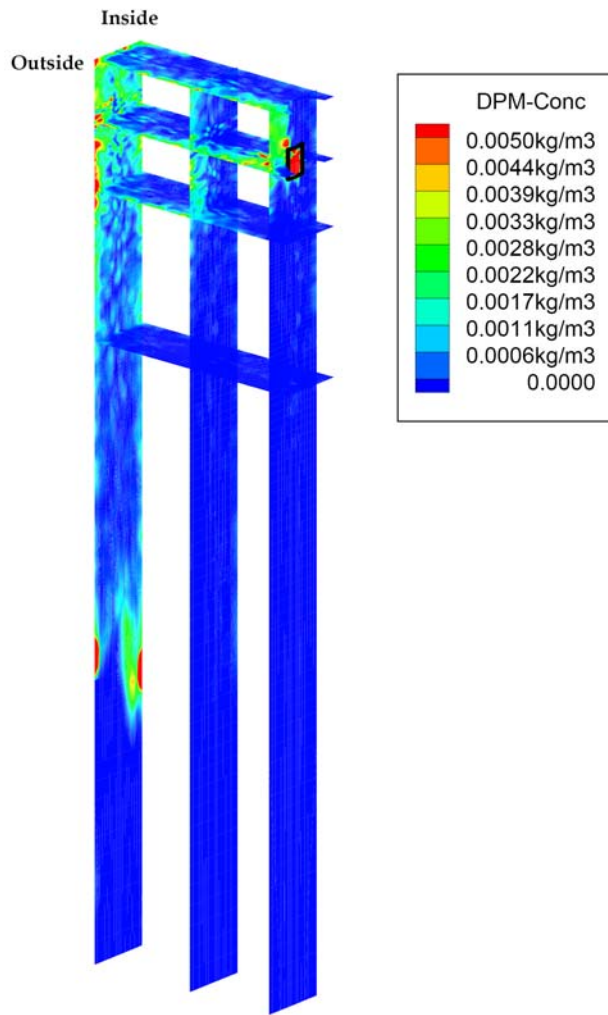


Figure 3.14 Three dimensional view of bubble concentration contours at 50sec after argon gas injection with 5SLPM

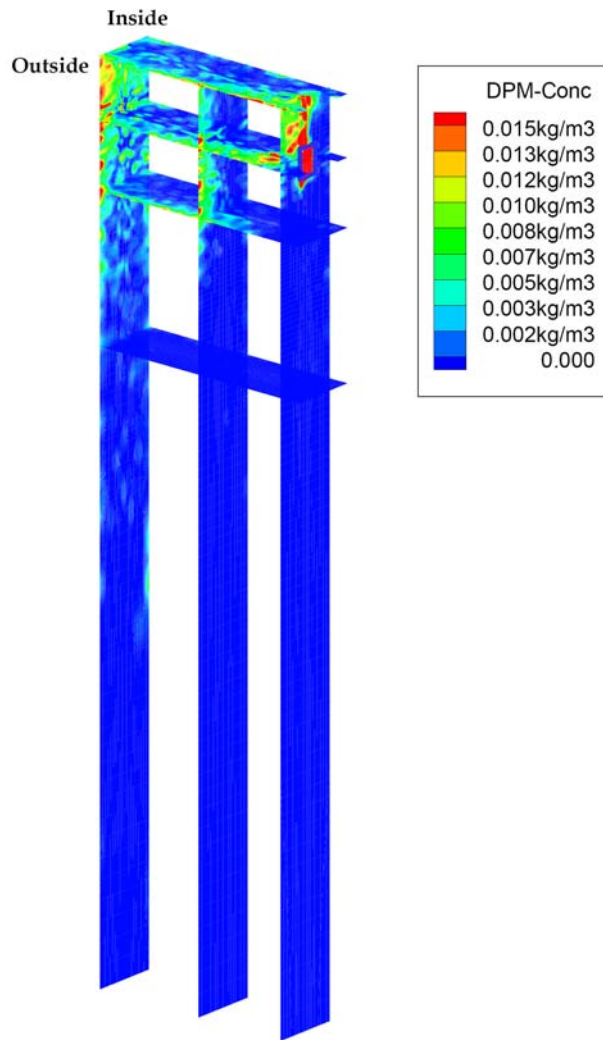


Figure 3.15 Three dimensional view of bubble concentration contours at 50sec after argon gas injection with 9SLPM

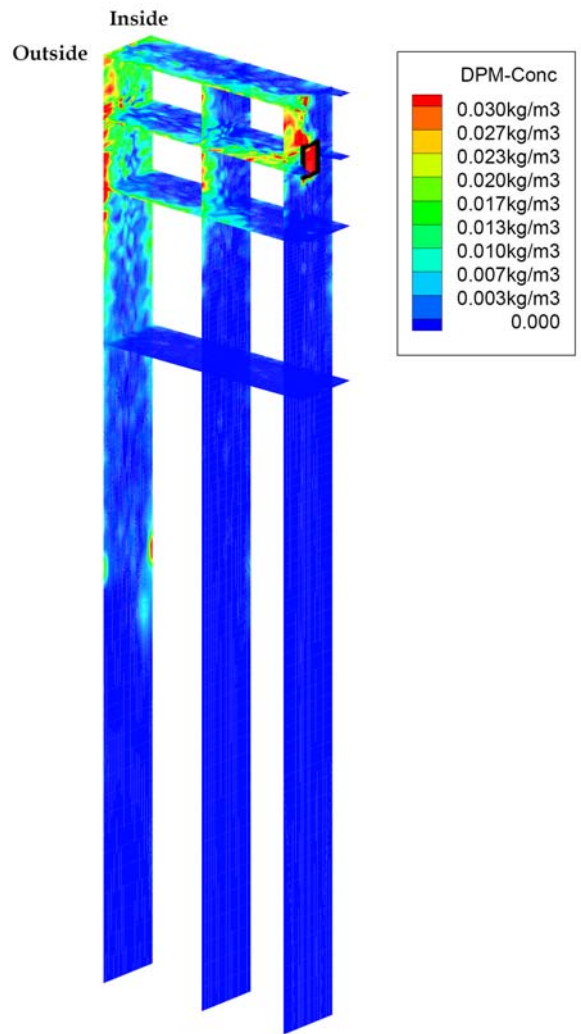


Figure 3.16 Three dimensional view of bubble concentration contours at 50sec after argon gas injection with 11SLPM

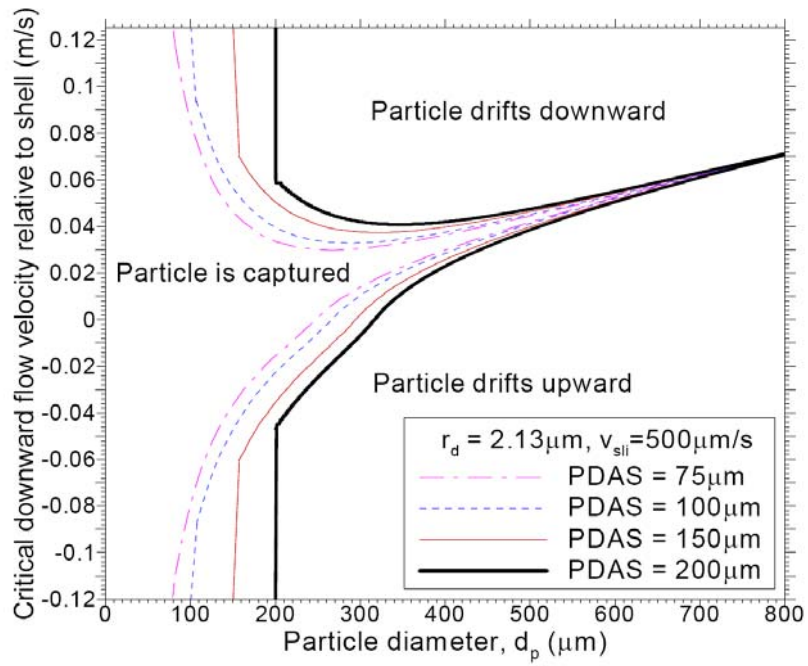


Figure 3.17 Cross-flow velocity effect on capture of particle[78]

3.6 Summary

A study using water model experiments, plant measurements and computational models of multiphase fluid flow has revealed that bubbles and inclusions in continuous-cast steel are entrapped due to asymmetric flow inside the nozzle as follows:

1. Bubbles form upon injection of gas through each active site in the UTN in proportion to the gas flow rate, downward liquid velocity, and fluid properties. A method to predict bubble mean size and distribution is shown and validated.
2. Bubbles exit the upper outside-radius corner of the nozzle outlet ports, owing to asymmetric flow inside the nozzle. In the present case, the asymmetry was caused by the slide-gate orientation, opening to cause more steel flow down the inside-radius side of the nozzle.
3. Bubbles rise up the outside radius of mold, increasing gas concentration at the outside radius, causing buoyancy-driven flow to move up and across the top surface towards the inside radius.
4. Particles and bubbles trapped in the flow down the inside radius may become suspended at the solidification front, allowing time for entrapment. This explains the increase number of large particles found on the inside radius.

This mechanism has the following implications:

1. Increasing gas flow rate causes more flow towards the inside radius, as confirmed by the nail board dip test measurements.
2. Straight (vertical) mold walls and strand extend until the solidifying shell is ~30mm thick. The increased inside-radius entrapment within

this thickness indicates that the defects are not due to machine curvature, but due to the asymmetric flow.

3. Asymmetric steel flow towards one side of the nozzle increases the frequency and size of particles entrapped on that the opposite side of the strand and decreases entrapment on the other strand face. The asymmetry may reverse periodically owing to chaotic turbulent variations. Efforts to limit the entrapment of large particles should focus on preventing asymmetric effects that cause downward flow from the top surface of the mold.

CHAPTER 4. Conclusions

In order to increase the understanding of the fluid flow and particle transportation phenomena in the nozzle and the mold, three different approaches have been studied in this work.

The analysis of nail board dip tests have been used to discretized the surface flow pattern in the mold with different gas flow rate at UTN. The shape and height of skull on the nail implies the flow direction, flow intensity, and meniscus profile. Increasing gas flow rate, it appears to change the direction from double-roll pattern, which is generally directed from the narrow face toward the SEN, to single-roll pattern which is generally directed from the SEN toward the narrow face. With higher gas flow rate, higher flow intensity is observed near the SEN and center region, due to the uplifting buoyancy force of the bubbles on the flow at those regions, and the flow direction across the top surface is asymmetrical flow which is mainly directed from the outside radius towards the inside radius at higher gas flow rates.

The analysis of entrapped particles in continuously-cast slabs has been utilized in this work to develop the location of entrapped particles and their associated formation mechanism. The subsurface hook defect, which entraps argon bubbles and alumina inclusion, explains the characteristic of subsurface region in the slab. Deepest hook related to slab surface quality appears at the slab corners, owing to further meniscus solidification, likely due to the colder liquid in this region. The internal defect detected by ultra-sonic analysis up to ~60mm from slab surface, the distribution of entrapped particles with higher gas flow rate at UTN is very asymmetrical. The reason of asymmetric distribution with higher gas flow rate causes from asymmetric flow between wide faces in the mold, corresponding with results of nail board dip tests.

The water model experiment has been developed to investigate the initial bubble behavior with porous MgO refractory in this study to simulate the

actual dolomite refractory. The gas is injected by pores on inner wall surface through a lot of connected pores inside porous MgO refractory. In this work, the active site which indicates the actual site exiting bubble on the inner surface of porous refractory was used for the effect of refractory properties on the initial bubble behavior both stagnant and downward-flowing water. The bubble formation depends primarily on the velocity of the flowing liquid and secondarily on the gas flow rate. The relationship of the mean gas flow rate per active site between water model and steel caster is investigated, and it gives new insight of similarity of water model experiment and steel system to aid in the design of future water models. Bubble size in a real nozzle is predicted using a previous analytical model, as confirmed measurements and its distribution is developed using a Rosin-Rammler distribution function with parameters taken from measurements. The bubble size and distribution can be used for the input data of computational multiphase simulation in the nozzle with more accuracy.

The computational models of multiphase fluid flow combined with water model experiments, and plant measurements has revealed that argon bubbles and inclusions in continuous-cast steel slabs are entrapped due to asymmetric flow inside the nozzle. Bubbles exit the upper outside-radius corner of the nozzle outlet ports, owing to asymmetric flow inside the nozzle, likely due to the slide-gate orientation, opening to cause more steel flow down the inside-radius side of the nozzle. Therefore, bubbles rise up the outside radius of mold, increasing gas concentration at the outside radius, causing buoyancy-driven flow to move up and across the top surface towards the inside radius. Particles and bubbles trapped in the flow down the inside radius may become suspended at the solidification front, allowing time for entrapment. This explains the increase number of large particles found on the inside radius. Efforts to limit the entrapment of large particles should focus on preventing

asymmetric effects that cause downward flow from the top surface of the mold.

Study combined with three approaches including plant measurements, water model experiments, and computational modeling shows the phenomena of nozzle and mold. At lower gas flow rate condition at UTN, the bubble size is small and the flow at the surface in the mold is almost symmetrical causing symmetric defect distribution in slab, as confirmed by both plant measurements and computational modeling based on water model experiment. The distribution of entrapped particles in slabs shows the symmetrical, which is affected by nozzle flow directly. Otherwise, at higher gas flow rate at UTN, the bubble size is bigger, and the flow at the surface in the mold is asymmetrical toward inside radius wide face causing asymmetric defect distribution in slab, as confirmed by both plant measurements and computational modeling based on water model experiment. These methods are more effective for the investigation of the defect formation related to fluid flow with reliability.

References

1. *World Steel in Figures*. 2006, International Iron and Steel Institute: Brussels, Belgium.
2. B. G. Thomas, *Modeling of the continuous casting of steel-past, present, and future*. Metallurgical and Materials Transactions B-Process Metallurgy and Materials Processing Science, 2002. **33**(6): p. 795-812.
3. B. G. Thomas, X. Huang, and R.C. Sussman, *Effect of Argon Gas on Fluid Flow in a Continuous Slab Casting Mold*. Metall. Trans. B, 1994. **25B**(4): p. 527-547.
4. A. Theodorakakos and G. Bergeles, *Numerical investigation of the interface in a continuous steel casting mold water model*. Metallurgical and Materials Transactions B-Process Metallurgy and Materials Processing Science, 1998. **29**(6): p. 1321-1327.
5. D. Gupta and A.K. Lahiri, *Water-Modeling Study of the Surface Disturbances in Continuous Slab Caster*. Metallurgical and Materials Transactions B-Process Metallurgy and Materials Processing Science, 1994. **25**(2): p. 227-233.
6. B. G. Thomas, D. Lui, and B. Ho, *Effect of Transverse and Oscillation Marks on Heat Transfer in the Continuous Casting Mold*, in *Sensors in Materials Processing: Techniques and Applications*, V. Viswanathan, R.G. Reddy, and J.C. Malas, Editors. 1997, TMS, Warrendale, PA: Orlando, FL. p. 117-142.
7. G.D. Lawson, et al., *Prevention of Shell Thinning Breakouts Associated with Widening Width Changes*, in *Steelmaking Conf. Proc.* 1994, ISS,

- Warrendale, PA: Chicago, IL. p. 329-336.
8. T. J. H. Billany, et al., *Surface Cracking in Continuously Cast Products*. Ironing and Steelmaking, 1991. **18**(6): p. 403-410.
 9. W. H. Emling, et al., *Subsurface Mold Slag Entrainment in Ultra-Low Carbon Steels*, in *Steelmaking Conf. Proc.* 1994, ISS, Warrendale, PA: Chicago, IL. p. 371-379.
 10. J. Herbertson, et al., *Modelling of Metal Delivery to Continuous Casting Moulds*, in *Steelmaking Conf. Proc.* 1991, ISS, Warrendale, PA: Washington, D.C. p. 171-185.
 11. H. J. Shin, *Study on the initial solidification behavior with etched subsurface hook structure in ultra-low carbon steel slabs* in *Materials Science and Engineering*. 2006, Pohang University of Science and Technology: Pohang.
 12. Bommaraju, R., et al., *Design, Development and Application of Mold Powder to Reduce Slivers*. *Iron & Steelmaker*, 1992. **19**(4): p. 21-27.
 13. Birat, J.-P., et al. *The continuous casting mold: A basic tool for surface quality and strand productivity*. in *Steelmaking Conference Proceedings*. 1991. Washington, DC: ISS-AIME, Warrendale, PA.
 14. H.-J. Shin, et al. *Effect of Mold Oscillation on Powder Consumption and Hook Formation in Ultra Low Carbon Steel Slabs*. in *AISTech 2004*. 2004. Nashville, TN: The Association for Iron & Steel Technology.
 15. H.-J. Shin, et al. *Analysis of Hook Formation Mechanism in Ultra Low Carbon Steel using CONID Heat Flow Solidification Model*. in *MS&T 2004*. 2004. New Orleans, LA: The Association for Iron and Steel

Technology (AISTech) and TMS.

16. Y. Shirota. in *143rd-144th Nishiyama Memorial Seminar*. 1992. Tokyo: ISIJ.
17. P. K. Tripathy, et al., *Migration of stab defects during hot rolling*. *Ironmaking & Steelmaking*, 2006. **33**(6): p. 477-483.
18. T. Miyake. in *AISTech 2006*. 2006. Cleveland, OH.
19. K. Mukai, M. Zeze, and T. Morohoshi, *Motion of fine particles under interfacial tension gradient in relation to solidification of steel*. *Solidification and Gravity IV in Materials Science Forum*, 2006. **508**: p. 211-220.
20. B. G. Thomas, et al., *Comparison of four methods to evaluate fluid velocities in a continuous slab casting mold*. *ISIJ International*, 2001. **41**(10): p. 1262-1271.
21. R. Sobolewski and D.J. Hurtuk, *Water Modeling of Slab Caster Flow Conditions*, in *2nd Process Technology Conf. Proc.* 1982, Iron and Steel Society, Warrendale, PA. p. 160-165.
22. D. Gupta and A.K. Lahiri, *A water model study of the flow asymmetry inside a continuous slab casting mold*. *Metallurgical and Materials Transactions B-Process Metallurgy and Materials Processing Science*, 1996. **27**(5): p. 757-764.
23. D. Gupta, S. Chakraborty, and A.K. Lahiri, *Asymmetry and oscillation of the fluid flow pattern in a continuous casting mould: A water model study*. *ISIJ International*, 1997. **37**(7): p. 654-658.

24. S. Sivaramakrishnan, B.G. Thomas, and S.P. Vanka, *Large Eddy Simulation of Turbulent Flow in Continuous Casting of Steel*, in *Materials Processing in the Computer Age*, V. Voller and H. Henein, Editors. 2000, TMS, Warrendale, PA. p. 189-198.
25. M. B. Assar, P. H. Dauby, and G.D. Lawson, *Opening the Black Box: PIV and MFC Measurements in a Continuous Caster Mold*, in *Steelmaking Conf. Proc.* 2000, ISS, Warrendale, PA: Pittsburgh, PA. p. 397-411.
26. Bai Hua, B.G.T., *Effects of Clogging, Argon Injection, and Continuous Casting Conditions on Flow and Air Aspiration in Submerged Entry Nozzles*. Metallurgical and Materials Transactions B, 2001. **32**(4): p. 707-722.
27. Bai Hua, B.G.T., *Turbulent Flow of Liquid Steel and Argon Bubbles in Slide-Gate Tundish Nozzles: Part I. Model Development and Validation*. Metallurgical and Materials Transactions B, 2001. **32**(2): p. 253-267.
28. Bai Hua, B.G.T., *Turbulent Flow of Liquid Steel and Argon Bubbles in Slide-Gate Tundish Nozzles: Part II. Effect of Operation Conditions and Nozzle Design*. Metallurgical and Materials Transactions B, 2001. **32**(2): p. 269-284.
29. M. Yao, et al., *Three Dimensional Analysis of Molten Metal Flow in Continuous Casting Mould*. Trans. Iron Steel Inst. Japan, 1984. **24**(2): p. s211.
30. T. Shi, *Effect of Argon Injection on Fluid Flow and Heat Transfer in the Continuous Slab Casting Mold*, in *Dept. Mech. & Eng.* 2001, University of Illinois at Urbana-Champaign: Urbana.

31. P.H. Dauby, W.H. Emling, and R. Sobolewski. *Lubrication in the mold: A Multiple Variable System*. 1986.
32. R. McDavid and B.G. Thomas, *Metall. Trans. B*, 1996. **27B**: p. 672-85.
33. Thomas, B.G., *Chapter 14. Fluid Flow in the mold*, in *Making, Shaping and Treating of Steel*, A.W. Cramb, Editor. 2003, AISE Steel Foundation: Pittsburgh, PA.
34. B. Rietow and B. G. Thomas, *Using nail board experiments to quantify surface velocity in the CC mold*, in *AISTech 2008*. 2008: Pittsburgh, PA.
35. Takeuchi, E. and J.K. Brimacombe, *The formation of oscillation marks in the continuous casting of steel slabs*. *Met. Trans B*, 1984. **15B**(Sept): p. 493-509.
36. Emi, T., et al., *Influence of physical and chemical properties of mold powders on the solidification and occurrence of surface defects of strand cast slabs*. *Proceedings of National Open Hearth and Basic Oxygen Steel Conference*, 1978. **61**: p. 350-361.
37. Schmidt, K.D., et al., *Consequent improvement of surface quality by systematic analysis of slabs*. *Steel Research International*, 2003. **74**(11-12): p. 659-666.
38. Birat, J., et al., *The Continuous Casting Mold: A Basic Tool for Surface Quality and Strand Productivity*, in *Mold Operation for Quality and Productivity*, A.W. Cramb and E. Szekeres, Editors. 1991, Iron and Steel Society, Warrendale, PA. p. 3-14.
39. Brimacombe, J.K. and K. Sorimachi, *Crack Formation in the Continuous Casting of Steel*. *Metall. Trans. B*, 1977. **8B**: p. 489-505.

40. Takeuchi, E. and J.K. Brimacombe, *Effect of Oscillation-Mark Formation on the Surface Quality of Continuously cast Steel Slabs*. Met. Trans B, 1985. **16B**(Sept): p. 605-625.
41. Harada, S., et al., *A formation mechanism of transverse cracks on CC slab surface*. ISIJ International, 1990. **30**(4): p. 310-316.
42. Shin, H.-J., et al. *Analysis of Hook Formation Mechanism in Ultra Low Carbon Steel using CONID Heat Flow - Solidification Model*. in *Materials Science & Technology 2004*. 2004. New Orleans, LA: TMS, Warrendale, PA.
43. J. Sengupta, et al., *A New Mechanism of Hook Formation during Continuous Casting of Ultra-low-carbon Steel Slabs*. Metallurgical and Materials Transactions A, 2006. **37A**(No. 5): p. 1597-1611.
44. J. Sengupta, et al., *Micrograph evidence of meniscus solidification and sub-surface microstructure evolution in continuous-cast ultralow-carbon steels*. Acta materialia, 2006. **54**(No. 4): p. 1165-1173.
45. H. Yamamura, Y. Mizukami, and K. Misawa, *Formation of Solidified Hook-like Structure at the Subsurface in Ultra Low Carbon Steel*. ISIJ International, 1996. **Supplement**: p. S223-226.
46. J. Sengupta, et al., *Micrograph evidence of meniscus solidification and sub-surface microstructure evolution in continuous-cast ultralow-carbon steels*. Acta Materialia, 2006. **54**(4): p. 1165-1173.
47. H. Fredriksson and J. Elfsberg, *Thoughts about the Initial Solidification Process during Continuous Casting of Steel*. Scandinavian Journal of Metallurgy, 2002. **31**(No. 5): p. 292-297.

48. Bikerman, J.J., *Physical surfaces*. 1970, New York (NY): Academic Press.
49. B. G. Thomas and X. Huang. *Effect of Argon Gas on Fluid Flow in a Continuous Slab Casting Mold*. in *76th Steelmaking Conf. Proc.* 1993. Dallas, TX: Iron and Steel Society, Warrendale, PA.
50. Go-Gi Lee, et al., *Microstructure near corners of continuous-cast steel slabs showing three-dimensional frozen meniscus and hooks*. *Acta Materialia*, 2007.
51. Sengupta, J., et al., *Micrograph evidence of meniscus solidification and sub-surface microstructure evolution in continuous-cast ultralow-carbon steels*. *Acta Materialia*, 2006. **54**(4): p. 1165-1173.
52. Tsuge, H., in *Encyclopedia of Fluid Mechanics*, G.P. Co., Editor. 1986: Houston, TX. p. 191-232.
53. N. Rabiger and A. Vogelpohl, in *Encyclopedia of Fluid Mechanics*, G.P. Co., Editor. 1986: Houston, TX. p. 58-88.
54. R. Clift, J. R. Grace, and M. E. Weber, *Bubbles, Drops and Particles*. 1978, New York: Academic Press, INC.
55. R. Kumar and N. R. Kuloor, in *Advances in Chemical Engineering*, A. Press, Editor. 1970: New York. p. 255-368.
56. H. Bai and B.G. Thomas, *Bubble Formation during Horizontal Gas Injection into Downward-Flowing Liquid*. *Metallurgical and Materials Transactions B*, 2001. **32**(6): p. 1143-1159.
57. Z. Wang, K. Mukai, and D. Izu, *Influence of wettability on the behavior*

- of argon bubbles and fluid flow inside the nozzle and mold.* ISIJ International, 1999. **39**(2): p. 154-163.
58. R. Nunnington, *Private Communication*. 2005: Urbana-Champaign, IL.
 59. G. A. Irons and R. I. L. Guthrie, *Bubble formation at nozzles in pig iron.* Metal. & Material Trans. B., 1978. **9**(2): p. 101-110.
 60. Brian G. Thomas and Z. Hashisho, *Argon Gas Flow through Nozzle Refractories*, in *CCC Annual report*, B.G. Thomas, Editor. 2005: Champaign.
 61. H. Bai, *Argon Bubble Behavior in Slide-gate Tundish Nozzles during Continuous Casting of Steel Slabs*, in *Dept. Mech. Eng.* 2000, University of Illinois at Urbana-Champaign: Urbana.
 62. *FLUENT6.2-Manual*, I. Fluent, Editor. 2005: Lebanon, NH.
 63. Z. Wang, et al., CAMP-ISIJ, 1998. **11**: p. 24.
 64. Z. Wang, et al., CAMP-ISIJ, 1997. **10**: p. 68.
 65. J. Boussinesq, Acad. Sci. Inst. Fr., 1877. **23**: p. 46-50.
 66. Wilcox, D.C., in *Turbulence Modeling for CFD*. 2000, DCW Industries Inc. p. 103-218.
 67. J. C. Rotta, *Statistiche Theorie nichthomogener Turbulenz.* Z. Physik, 1951. **29**: p. 547-572.
 68. B. J. Daly and F. H. Harlow, *Transport Equations in Turbulence.* Phys. Fluids, 1970. **13**: p. 2634-2649.

69. M. M. Gibson and B. E. Launder, *Ground Effects on Pressure Fluctuations in the Atmospheric Boundary Layer*. J. Fluid Mech., 1978. **86**: p. 491-511.
70. *FLUENT 6.2*. 2003, Fluent Inc.: Lebanon, New Hampshire.
71. C.Crowe, M.Sommerfeld, and Y.Tsinji, *Multiphase Flows with Droplets and Particles*. 1998, CRC Press. p. 23-95.
72. P.G. Saffman, *The Lift on a Small Sphere in a Slow Flow*. Journal of Fluid Mechanics, 1965. **22**: p. 385-400.
73. J. B. McLaughlin, *Inertial migration of small sphere in linear shear flows*. Journal of Fluid Mechanics, 1991. **224**: p. 261-274.
74. R. Mei, *An Approximate Expression for the Shear Lift Force on a Spherical-Particle at Finite Reynolds-Number*. International Journal of Multiphase Flow, 1992. **18**(1): p. 145-147.
75. D. Creech, *Computational Modeling of Multiphase Turbulent Fluid Flow and Heat Transfer in the Continuous Slab Casting Mold*, in *Mechanical and Industrial Engineering*. 1999, University of Illinois at Urbana-Champaign: Urbana.
76. H. Bai and B.G. Thomas, *Turbulent Flow of Liquid Steel and Argon Bubbles in Slide-Gate Tundish Nozzles: Part I. Model Development and Validation*. Metallurgical and Materials Transactions B, 2001. **32**(2): p. 253-267.
77. Quan Yuan, Brian G. Thomas, and S.P. Vanka, *Study of Transient Flow and Particle Transport in Continuous Steel Caster Molds: Part II. Particle Transport*. Metall. Trans. B, 2004. **35B**(4): p. 703-714.

78. Q. Yuan, B.G. Thomas, and S.P. Vanka, *Study of Transient Flow and Particle Transport during Continuous Casting of Steel Slabs, Part 2. Particle Transport*. *Metal. & Material Trans. B.*, 2004. **35B**(4): p. 703-714.

Summary (in Korean)

Acknowledgments

Curriculum Vitae

Full Name as in Passport: Lee Go-Gi
(*Family name underlined*)
Date of Birth: 27 January, 1977
Place of Birth: Yosu, South Korea
Nationality: Korean

Education

Doctor of Philosophy in Department of Materials Science and Engineering,
Pohang University of Science and Technology, South Korea (2008. 8)

Bachelor of Science in Division of Advanced Materials Science and
Engineering, Hanyang University, South Korea (2002. 2)

Research experiences

Visiting Scholar, Department of Mechanical Science and Engineering,
University of Illinois at Urbana-Champaign, IL, USA (2006. 2 ~ 2008. 3)

Requesting Researcher, Steelmaking Research Group, POSCO Research
Laboratories, South Korea (2003. 9 ~ 12)

Requesting Researcher, Steelmaking Research Group, POSCO Research
Laboratories, South Korea (2003. 6 ~ 8)

Publications

Journal papers

1. Go-Gi Lee, Brian G. Thomas, Seon-Hyo Kim, Ho-Jung Shin, Seung-Kwan Baek, Choon-Haeng Choi, Dong-Su Kim and Sung-Jong Yu, "Microstructure near corners of continuous-cast steel slabs showing

- three-dimensional frozen meniscus and hooks," *Acta Materilia*, Vol. 55, Iss. 20, December 2007, pp. 6705-6712
2. Sung-Kwang Kim, Ho-Jung Shin, Go-Gi Lee, "Improvement of slab subsurface quality by change of casting parameters in continuous-cast ultra-low-carbon steels," *SEAIISI Quartely* (South East Asia Iron and Steel Institute), Vol. 36, Iss. 3, May 2007, pp. 19-29
 3. Ho-Jung Shin, Seon-Hyo Kim, Brian G. Thomas, Go-Gi Lee, Je-Min Park and Joydeep Sengupta, "Measurement and Prediction of Lubrication, Powder Consumption, and Oscillation Mark Profiles in Ultra-low Carbon Steel Slabs," *ISIJ Int.*, Vol. 46, No. 11, 2006, pp. 1635-1644
 4. Joydeep Sengupta, Brian G. Thomas, Ho-Jung Shin, Go-Gi Lee and Seon-Hyo, "A New Mechanism of Hook Formation during Continuous Casting of Ultra-Low-Carbon Steel Slabs," *Metallurgical and Materials Transactions A*, Vol. 37, No. 5, 2006, pp. 1597-1611
 5. Ho-Jung Shin, Go-Gi Lee, Wung-Yuel Choi, Sin-Myoung Kang, Jang-Hum Park, Seon-Hyo Kim and Brian G. Thomas, "Effect of Mold Oscillation on Powder Consumption and Hook Formation in Ultra Low Carbon Steel Slabs," *Iron & Steel Technology*, Iron & Steel Technology, Vol. 2, No. 9, 2005, pp. 56-59

Conference proceedings papers

1. Go-Gi Lee, Brian G. Thomas, Seon-Hyo Kim, Ho-Jung Shin, "Asymmetric Multi-phase Fluid Flow and Particle Entrapment in a Continuous Casting Mold," *AISTech 2008*, May 5-8, 2008, Pittsburgh, PA, USA
2. Chen Tao, Go-Gi Lee, Seon-Hyo Kim, "Water Model Simulation of Gas Injection into SEN of CC," 2007 CSM Annual Meeting, November 14-17, 2007, Chengdu, China
3. G. G. Lee, H. J. Shin, B. G. Thomas, S. H. Kim, D. S. Kim, S. J. Yu, "Microstructure near corners of continuous-cast steel slabs showing three-dimensional frozen meniscus and hooks", *AISTech 2007*, May 7-10, 2007, Indianapolis, IN, USA
4. Shin H.-J., B. G. Thomas, G. G. Lee, J. M. Park, C. H. Lee and S. H. Kim, "Analysis of Hook Formation Mechanism in Ultra Low Carbon Steel using CON1D Heat Flow - Solidification Model", *Materials Science & Technology 2004 (MS&T2004)*, Sept. 26-29, 2004, New Orleans, LA, USA, Vol. 2, pp. 11-26
5. Shin H.-J., G. G. Lee, W. Y. Choi, S. M. Kang, J. H. Park, S. H. Kim and B. G. Thomas, "Effect of Mold Oscillation on Powder Consumption and Hook Formation in Ultra Low Carbon Steel Slabs", *AISTech 2004* Nashville, TN, Sept. 15-17, 2004, Association Iron Steel Technology,

Presentations / Posters

1. 이고기, 김선호, 신호정 and B. G. Thomas, "연속주조공정의 주형 내부 비대칭 유동해석 및 결함분포에 관한연구," 2008년 대한금속·재료학회 춘계 학술대회, 대전, 2008
2. H-J. Shin, W-Y. Choi, J-M. Park, S-Y. Kim, J-H. Park, B.G. Thomas, G. G. Lee, S-H. Kim, "Estimation of hook depth calibrated with measured mean heat flux in plant," 6th ECCC, June 3-6, Riccione, Italy
3. G. G. Lee and B. G. Thomas, "Multi-Phase Asymmetric Fluid Flow & Inclusion Entrapment in the Slab Mold," 2007 Annual Meeting, Continuous Casting Consortium at UIUC, Urbana, Illinois, USA, Jun. 12, 2007
4. Go-Gi Lee, Ho-Jung Shin, Seon-Hyo Kim, Claudio Ojeda and Brian G. Thomas, "Investigation of oscillation marks and hook formation in ULC steels using metallurgical analysis and models", UIUC-Purdue Joint Conference on Solidification and Metals Processing Research, September 14th 2006, Urbana-Champaign, IL, USA
5. G. G. Lee and B. G. Thomas, "Hook Formation near Slab Corners and Prediction of Argon Gas Bubble Size in the Slab Casting Mold," 2006 Annual Meeting, Continuous Casting Consortium at UIUC, Urbana, Illinois, USA, Jun. 15, 2006
6. 황상택, 김선호, 이고기, 신호정, 김성광, "중탄소강에서 합금원소와 전열량 변화가 초기응고 거동에 미치는 영향," 2006년 대한금속·재료학회 추계 학술대회, 제주, 2006
7. Ho-Jung Shin, Go-Gi Lee, Seon-Hyo Kim, Joydeep Sengupta and Brian G. Thomas, "Investigation of oscillation marks and hook formation in ULC steels using metallurgical analysis," Joint Illinois-Purdue Symposium on Simulation of Solidification, July 7th 2005, Urbana-Champaign, IL, USA
8. S. H. Park, G. G. Lee, C. H. Park and S. H. Kim, "Growth and characterization of ZnO, ZnMgO film on sapphire by metal organic chemical vapor deposition," The 113rd Annual Meeting & Exhibition of The Minerals, Metals & Materials Society(TMS), 2004 TMS, Charlotte, NC, USA
9. 이고기, 신호정, 강신명, 김선호, 박제민, "연속주조 공정에서 극저탄소강의 코너부 분석을 통한 메니스커스부 관찰," 2004년 추계 금속학회, 대한금속재료학회, 부산, 2004

10. 이고기, 신호정, 강신명, 김선효, 박제민, “극저탄소강의 슬라브 코너부 분석을 통한 초기응고 형태 관찰,” 제 16회 포스코 철강기술 컨퍼런스, 포스코, 포항, 2004
11. 김성광, 신호정, 이고기, 김선효, “주조속도 변화에 따른 Hook 결함 발생기구에 대한 연구,” 2002년 추계 금속학회, 대한금속재료학회, 서울, 2002